Origin and kinematics of a basin-scale, non-polygonal, layer-bound normal fault system in the Levant Basin, eastern Mediterranean

Amir Joffe [1*], Christopher A-L. Jackson[1,2], Josh Steinberg[3], Rebecca E. Bell[1], Yizhaq Makovsky[4]

1. Basins Research Group (BRG), Department of Earth Science and Engineering, Imperial College London, South Kensington Campus, SW7 2BP, UK
2. Jacobs, Manchester, M15 4GU, UK
3. Ratio Energies, Tel-Aviv, Israel
4. Dr. Moses Strauss Department of Marine Geoscience, CSMS, University of Haifa, Haifa, Israel

*Corresponding author: amir.joffe18@imperial.ac.uk

Acknowledgments

We would like to thank Ratio Energies for their financial support of Amir Joffe's PhD and for providing the data for this study. We thank Ratio Energies partners, Delek Drilling and Chevron, for approving access to the data and the publication of this manuscript. We extend out thanks to Emerson for sponsoring Paradigm software to the Applied Marine Exploration Laboratory, University of Haifa. We would also like to thank Schlumberger for sponsoring Petrel software, and Geoteric for their academic licenses for Imperial College. Kul Karcz, Omri Shitrit, Yedidia Gellman, Or Bialik, and Mark Ireland for fruitful discussion during the preparations of this manuscript.

Data Availability Statement

The data is not publicly available due to confidentiality agreements.

Abstract

Polygonal, layer-bound normal faults can extend over very large areas (>2,000,000 km^2) of sedimentary basins. Best developed in very fine-grained rocks, these faults are thought to form during early burial in response to a range of diagenetic processes, including compaction and water expulsion. Local deviations from this idealised polygonal pattern are common; however, basin-scale, layer-bound faults with non-polygonal map-view are not well-documented and accordingly, their genesis is not well-understood. In this study we use 3D seismic reflection data, biostratigraphy, and well-logs from the Southern Levant Basin, offshore Israel, to develop an age-constrained seismic-stratigraphic framework and determine the geometry and kinematics of such basin-scale fault system. The faults tip-out downwards along an Eocene Unconformity, but unlike layer-bound faults in the Northern Levant Basin, they do not reach the base of the Messinian evaporites, instead tipping-out upwards at the top Langhian. On average, the faults in the Southern Levant Basin are 6.3 km long, have an average throw of 120 m, and consistently strike NW-SE. Throw-depth plots, accompanied by thickness changes, indicate that the faults accumulated growth strata during the Late Burdigalian, and are spatially and kinematically associated with a WSW-ESE-striking strike-slip fault. Unlike true polygonal faults, these faults propagated through ~2 km-thick sandstone-prone Oligocene-Miocene strata. Whereas previous studies from the Northern Levant Basin associate fault nucleation and growth with burial-related diagenesis, the sandstone-prone character of the Oligocene-Miocene suggests that this process cannot be readily applied to the Southern Levant Basin. Instead, we highlight potential tectonic events that occurred during and may have triggered thin-skinned extension at times of fault growth.

1. Introduction

Layer-bound normal faults (defined as faults that are vertically restricted within discrete stratigraphic units and do not offset the basement) are found in sedimentary rocks throughout the geological record. One of the most common types of layer-bound faults are polygonal faults. These low-displacement (<100 m) normal faults are found in >150 basins around the world, forming broadly polygonal plan-view systems covering extensive area (>2,000,000 km^2) (Cartwright, 2011). The faults are confined within discrete stratigraphic units called tiers, detached from the acoustic basement (Cartwright et al., 2003). These tiers are commonly tens to hundreds of meters thick, predominantly often dominated by very fine-grained, smectite-rich claystone or chalk, and are bounded by sandstone-prone units or other types of detachment layers (Cartwright and Lonergan, 1996; Cartwright and Dewhurst, 1998; Dewhurst et al., 1999). Their unique polygonal planform suggest growth within an isotropic stress field (i.e., $\sigma_{1\,(vertical)} > \sigma_2 = \sigma_3$), with this polygonal planform being highly sensitive to local changes in the prevailing stress regime (Roberts et al., 2015). For example, changes in host rock dip, and stress perturbations around salt diapirs, pockmarks, and even deep-water channels all can alter the faults polygonal planform, causing them to become locally aligned or radially disposed (Goulty, 2002, 2008; Ireland et al., 2011; Carruthers et al., 2013; Morgan et al., 2015). Even in these cases, fault nucleation and growth are assumed to be triggered by the same, early burial-related diagenetic process as inferred for true polygonal faults. Whereas their kinematics are fairly well understood, and there is a general agreement they form by post-burial diagenetic processes involving dewatering in fine-grained clays and chalk, the exact mechanism responsible for their development is still under debate (Cartwright and Lonergan, 1996; Goulty, 2008; Cartwright, 2011; Wrona et al., 2017; King and Cartwright, 2020).

One particularly striking example of a basin-scale (~70,000 km^2), non-polygonal layer-bound fault system, for which the diagenetic model has previously been proposed, is the "piano-key" fault system of the Levant Basin, eastern Mediterranean (Kosi et al., 2012; Ghalayini et al., 2017). Comprised of NW-striking, mostly non-polygonal, linear (i.e., one single dominant orientation) faults, this system covers the entire Levant Basin, displacing the >2 km thick Oligocene-Miocene strata (Ghalayini et al., 2017). By integrating seismic attribute analysis and throw measurements along the faults surface, the spatial and temporal evolution of the fault system has been analysed in the Northern Levant Basin (Figure 1) (Kosi et al., 2012; Hawie et al., 2013; Ghalayini et al., 2017; Ghalayini and Eid, 2020). On the basis of the faults layer-bound geometry, a small portion of polygonally-shaped faults in the system, and the lack of known extension events at times of presumed fault nucleation, Ghalayini et al. (2017) associated the piano-key faults with the same dewatering, diagenetic mechanism often inferred to drive polygonal fault nucleation and growth. The dominant NW strike of the piano-key faults reflected their development in an anisotropic (rather than isotropic) stress field (Ghalayini et al., 2014, 2017).

Piano-key faults are also documented in the Southern Levant Basin, displacing a thick sandstone-prone, Oligocene-Miocene sequence (see detailed description in sub-section 2.0) (Steinberg et al., 2011; Needham et al., 2017; Craik and Ben-Gai, 2019; Gouliotis, 2019; Karcz et al., 2019; Ortega et al., 2019). The presence of these layer-bound faults within the sandstone-bearing sequence challenges the application of the diagenetic model fault development for the

Southern Levant Basin. In this study we aim to propose a mechanical model for the formation of the unusual piano-key faults in the Southern Levant Basin by constraining their structural evolution, the lithological variability of the faulted sequence and the broader geo-dynamic setting of the basin at the time of fault formation. To do this we use high-quality, 3D seismic reflection data, chronostratigraphic markers, and well-logs from six offshore wells. This allows us to (1) create a detailed, age-constrained, stratigraphic framework; (2) constrain the lithological variability of the different units within the faulted Oligo-Miocene; (3) measure the geometrical properties of individual faults and the fault system as a whole; (4) determine the faults kinematics; (5) discuss possible mechanical models for the formation of the piano-key faults, while also considering the geo-dynamic events occurring at the basin during fault nucleation and growth. We argue that the previously proposed diagenetic mechanism may not be applicable in this specific case (Ghalayini et al., 2017; Ghalayini and Eid, 2020), and those late Miocene regional tectonic events which shaped the Levant Basin may have played a role. More generally, we also argue that the presence of layer-bound normal faults should not be taken to necessarily infer very fine-grained sedimentary sequences in the absence of well data. As shown here, such structures could be erroneously interpreted as polygonal faults formed in an anisotropic stress field (Ghalayini et al., 2017), while actually forming in a sandstone-prone host rock. Our new interpretation for the origin of these enigmatic basin-scale, non-polygonal (i.e., unidirectional) layer-bound normal fault systems encourage re-examination of the origin and kinematics of other unidirectional normal fault systems to see if they have similar origins. Finally, as these layer-bound faults 'fossilise' the strain distribution in sedimentary basins, they can help us reconstruct the regional stresses and geodynamics of these basins.

2. Geological Setting

The Levant Basin is located in the eastern Mediterranean and is bordered by the Cyprus subduction arc to the north, the Eratosthenes Seamount to the west, and the continental margin of Egypt, Israel, Lebanon, and Syria to the south and east (Figure 1A). We here follow the arbitrary division of the basin into the Southern and Northern Levant Basins approximately along the Israel-Lebanon maritime border (Ben-Gai, 2018) (Figure 1A). The basin's unique location within a triple-junction of the Eurasia, Arabia, and Africa plates means it evolved in response to a complex series of tectonic-stratigraphic events.

The basin initially formed in response to Permian, Triassic, and Early Jurassic rifting, associated with multi-phase, NW-SE-oriented extension, thinning of the continental crust and the formation of NE-SW-striking normal faults (Garfunkel and Derin, 1984; Garfunkel, 1998;

Gardosh and Druckman, 2006; Robertson, 2007; Gardosh, Druckman, Buchbinder, and Rybakov, 2008; Gardosh et al., 2010; Sagy et al., 2015; Granot, 2016). Following this, passive margin conditions prevailed until the Late Cretaceous, during which time a shallow marine carbonate platform was established along the basin margin (Garfunkel and Derin, 1984; Garfunkel, 1998; Gardosh and Druckman, 2006; Gardosh, Druckman, Buchbinder, and Rybakov, 2008; Gardosh and Tannenbaum, 2014). Late Cretaceous convergence between the African and Eurasian plates resulted in the formation of a north-dipping subduction zone along the Cyprus Arc (Robertson, 1998a; Gardosh, Druckman, Buchbinder, and Rybakov, 2008; Morag et al., 2016). Within the Southern Levant Basin, compressional stresses related to ongoing subduction caused large-scale folding above the pre-existing, rift-related normal faults (Krenkel, 1924; Freund, 1975; Cohen et al., 1990; Druckman, 1994; Garfunkel, 2004; Sagy et al., 2018). Forming part of the 'Syrian Arc' (Krenkel, 1924), these folds are most prominent onshore and along the basin's eastern margin, where high-amplitude, short wave-length anticlines are developed (i.e., 10-30 km long, 5-10 km wide, and an amplitude of >1 km) (Eyal, 1996; Walley, 1998; Gardosh, Druckman, Buchbinder, and Rybakov, 2008). This first pulse of Syrian Arc-related folding stopped by the Eocene, during a time characterised by deepening and the deposition of deep-water chalk and marls across much of the Middle East (Garfunkel, 1998; Ziegler, 2001; Bar et al., 2013; Sagy et al., 2018; Steinberg et al., 2018).

In addition to witnessing a second Syrian-Arc related folding event (Syrian Arc II) (Robertson, 1998a; Walley, 1998; Gardosh, Druckman, Buchbinder, and Calvo, 2008; Needham et al., 2017; Sagy et al., 2018), the Oligo-Miocene recorded a drastic change in depositional environment within the basin, from deep-water carbonates to deep-water clastics, resulting in the Eocene Unconformity (Steinberg et al., 2011). This change created drastic increase in sedimentation rates, peaking between ~24-12 Ma (~900 m/Myr), two orders of magnitude higher than the pre-Oligocene period (~5 m/Myr) (Torfstein and Steinberg, 2020). The cause for this drastic and immediate change was linked to a series of geodynamic events that exposed large expanses of previously submerged areas, which then formed significant clastic sediment sources. These events include: (1) regional uplift of the eastern margin that exposed the Arabian Plateau, initiating large-scale, NW-directed drainage system into the retreating Levant (Zachos et al., 2001; Ziegler, 2001; Gvirtzman et al., 2011; Bar et al., 2016; Faccenna et al., 2019); (2) regional doming south of the Levant basin, created by the Afar Plume, which elevated the Ethiopian Plateau (31-29 Ma) (Bosworth et al., 2015); (3) Red-Sea rifting, which was initiated by the Cairo Plume (23 Ma) (Bosworth et al., 2005, 2015); (4) the final stages of closure of the

Indian Ocean – Mediterranean Seaway (IOMS) in the Aquitanian (Bialik et al., 2019; Torfstein and Steinberg, 2020); (5) the activation of the Continental Margin Fault Zone along the Levant eastern margin in the Early Oligocene (Gvirtzman and Steinberg, 2012); (6) the development of the Dead Sea transform in the Burdigalian (Freund, 1975; Garfunkel, 1997; Segev et al., 2014; Nuriel et al., 2017); and (7) the local uplift of the Judea Hills, onshore Israel (Bar et al., 2013). It is not yet clear if or how all these events kinematically interacted, but it does highlight that during the Oligo-Miocene, the Levant Basin was tectonically very active, and that this activity could have influenced the formation and growth of the fault system considered here.

Restriction of the Atlantic-Mediterranean waterway during the Late Miocene (5.59 – 5.33 Ma) resulted with the Messinian Salinity Crisis and the accumulation of up to ~2.5 km thick evaporitic sequence in the Levant basin (Hsü et al., 1977; Krijgsman et al., 1999; Ryan, 2009). After Pliocene rise of the Judea Hills and the development of the Dead-Sea Transform, the easterly drainage system was disconnected from the Levant, making the River Nile the main sediment source to the basin (Garfunkel, 1981; Gardosh, Druckman, Buchbinder, and Calvo, 2008; Gardosh, Druckman, Buchbinder, and Rybakov, 2008; Gvirtzman et al., 2014, 2015; Bar et al., 2016; Zucker et al., 2019; Kanari et al., 2020).

2.1. The Piano Key Faults of the Northern Levant Basin

The piano-key fault system is composed of a NW-striking normal fault system that covers ~70,000 km^2 offshore Lebanon, Israel, and Cyprus (Ghalayini et al., 2017). Offshore Lebanon, in the Northern Levant Basin, the faults are bounded below by the Eocene Unconformity and above by the base of the Messinian evaporites, displacing the Oligo-Miocene sedimentary sequence (Kosi et al., 2012; Ghalayini et al., 2017; Ghalayini and Eid, 2020). Based on their geometry and how fault throw varies with depth, the faults in the system offshore Lebanon were divided into three main 'types' by Ghalayini and Eid (2020) (Figure 1). Type-1 (T1) faults are predominantly located in the deep basin (Figure 1A). They are tall (~3800 m), long (6-12 km), linear, strike NW, and have a maximum displacement of 200-350 m (Ghalayini and Eid, 2020) (Figure 1B). Throw vs depth analysis, which highlights the depth of fault nucleation as a function of maximum throw, revealed two throw maxima separated by a local minimum, creating a "B-Type" profile (Muraoka and Kamata, 1983; Ghalayini et al., 2017). The analysis indicates that T1 faults had nucleated in separate tiers, later connecting by fault tip propagation (Figure 1B). The presence of growth strata in the 'Lower-Middle Miocene Interval' suggests faults breached the surface during the Early-Middle Miocene (Reiche et al., 2014), even though, we note, the faults could have nucleated at greater structural depths. Found in the northernmost part of the basin, adjacent to the Latakia Ridge, Type-2 (T2) faults are small (~1,000 m tall), short (2-3 km in length), and have smaller displacements than T1 faults (<60 m). Unlike T1, T2 faults have no observable growth strata, and their throw-depth analysis creates a symmetrical, "C-type" profile that lacks any local minima (Muraoka and Kamata, 1983; Ghalayini and Eid, 2020) (Figure 1B). Unlike the other types of faults, T2 faults are not co-linear in planform, but rather form a semi-polygonal planform (Figure 1A). Type-3 (T3) faults are linear, striking NW-SE. They are found along the eastern basin margin and do not displace the Eocene Unconformity or the base-Messinian (Ghalayini and Eid, 2020) (Figure 1B) being the smallest faults in the basin, i.e., they are <800 m tall, have <90 m of displacement, and are <3 km in length. T3 faults are characterised by "C-type" throw profiles and lack growth strata, similar to the T2 faults (Ghalayini and Eid, 2020).

The vast areal extent of the faults, alongside their layer-bound character and the polygonal planform of the T2 faults, led Ghalayini et al. (2017) to suggest they formed due to compaction and dewatering during shallow burial (e.g., Cartwright, 2011). In the absence of borehole data, these authors inferred that the faults developed in a mudstone-dominated, very fine-grained sedimentary sequence, typical of polygonal fault systems. They argued that the throw-minimum on the T1 faults and their "B-type" throw-depth profiles is associated with a sandstone-prone, basin floor fan (Ghalayini and Eid, 2020) (Figure 1C). Similar observations were made offshore Norway, both Ormen Lange Field, Møre Basin (e.g., Stuevold et al., 2003; Möller et al., 2004), and in the exploration well 35/9-3T2 located in the Måløy Basin (Jackson et al., 2004). In the case of the latter, a 92 m-thick sandstone-dominated body separated two mudstone-dominated tiers of polygonal faults, leading to a local minimum on throw-depth profiles (Jackson et al., 2014).

3. Dataset

The available dataset consists of seven deep-water wells, and one 3D Pre-Stack Depth Migrated (PSDM) seismic reflection volume covering 2355 km^2 in water depth of ~1.5 km offshore Israel (Figure 2A). The seismic data were acquired in 2009 and processed in 2010 by Petroleum Geo-Services. Reprocessing of the survey in 2019 by WesternGeco focused on the faulted Oligo-Miocene sequence, with a final bin size of 25x25 m. Inlines and crosslines are oriented NE-SW and NW-SE respectively (i.e., parallel, and perpendicular to the faults orientation). The seismic data are zero phase, 'normal' SEG polarity where a positive amplitude peak indicate an increase in acoustic impedance with depth (red in figures), and a negative amplitude troughs indicate a decrease in acoustic impedance (blue in figures).

The available wells targeted the Oligo-Miocene sequence, with X-2 terminating just above the faulted sequence. X-1 is the deepest well, reaching as deep as the Eocene unconformity (i.e., near the basal tips of the studied faults; Figure 2C). We had access to gamma-ray (GR), Neutron, Density logs (all three measured every 10-15 cm, depending on the well), computed volume of shale (Vsh) (see Methodology), cutting samples, and lithostratigraphic markers.

4. Methodology

We used lithostratigraphic markers, and chronostratigraphic data from dated cutting samples (Torfstein and Steinberg, 2020) to constrain the age of nine sub-evaporite reflections (Figure 2B). The deepest reflection mapped in this study was not penetrated by the wells, but following other seismic-stratigraphic frameworks, which correlated onshore data to the shallow offshore in the Southern Levant Basin (Gardosh et al., 2008b; Steinberg et al., 2011, 2018), we interpret it as the Upper Cretaceous Unconformity (previously labelled 'Senonian Unconformity'), based on its characteristic seismic expression (Steinberg et al., 2018) (Figure 2B). We also used spectral decomposition to highlight the subtle structural elements, most importantly the WSW-ENE-striking fault and its associated splays. Spectral decomposition involves decomposing the seismic reflection data into three frequency-band limited copies. Then the seismic amplitude envelopes are mapped from each copy along the interpreted structural surface and blended as red, green, and blue channels, respectively, to form a single composed full colour map. The obtained spectral decomposition maps highlight primarily frequency modulated seismic tuning due to subtle resolution thickness changes along the interpreted surfaces and are useful for delineating fine geological structure (Partyka et al., 1999; Othman et al., 2016). More specifically we here used the Geoteric HDFD spectral decomposition workflow which further enhance colour resolution and vertical resolution within the RGB blend (e.g., Eckersley et al., 2018).

The Oligo-Miocene succession comprises three (from youngest to oldest) main units: (i) smectite-rich mudstone, which contains thin sandstone beds; (ii) marls, which contain thin beds of smectite-rich mudstone; and (iii) a mud-rich sandstone, which forms the host rock to the fault system studied here (see Section 5.1. for further details). Given these units are all located below a thick, halite-dominated unit, a well-log-only analysis of their detailed composition is potentially problematic. This was highlighted by Christensen and Powers (2013), who raised two main issues based on their study of the nearby Tamar gas field. First, contamination of the rock units by hypersaline, barite-rich, water-based drilling fluids, which were used to drill through the Messinian evaporites and subsequently used to hinder swelling of smectite-rich mudstones units. Second, in most cases a relatively thick, sandstone-poor and fully resolved by well-logs mudstone located either directly above or below the depth of interest is used to as a baseline for 100% clay-content. However, the bounding mudstones in our study area are marls, rather than the clay-rich mudstone which comprises the faulted sequence of interest. Additionally, the faulted mud-rich layers within the overall heterolithic sub-salt sequence may also be too thin to be fully resolved by the logging tools when compared to the bounding marls-mudstone sequence, causing a traditional GR-based analysis to overestimate shale volumes. Another commonly used technique to differentiate between mudstone and sandstone is the cross-over between Neutron and Density logs (i.e., in the case of sandstone, neutron logs are deflected to the right and density logs are deflected to the left; see Figure 3). An issue arises here as these logs were mostly measured within the faulted, gas-prone, mud-rich sandstone unit, and are therefore affected by the gas content. The gas content causes underestimation of the pore-space within the rocks, and therefore affects the separation of the neutron and density logs, inhibiting a log-based lithological interpretation (see overview by Rider and Kennedy, 2014). In a similar way to the GR log, the Natural Gamma Ray Spectrometry (NGS) log also measures the natural radioactivity emitted from rocks, but unlike a GR log it also breaks the radioactive energy into the three main radioactive elements (i.e., Potassium (K), Thorium, and Uranium). This allows for potentially better minerology identification, but as the drilling fluid was high in Potassium, it masks the real rock minerology.

To overcome these difficulties, Christensen and Powers (2013) suggest Nuclear Magnetic Resonance (NMR) can be used to correlate between the “clay-bound water” and the total porosity to create a so-called ‘Volume of Shale’ log (Vsh). Once the Vsh log was calculated, it was correlated to a GR baseline so that sandstone and mudstone could be differentiated. In areas where neutron and density readings were not affected by gas, the separation between these two logs (i.e., see above) also helped guide the Vsh log-driven lithological analysis.

In our study we used a similar analysis to that outlined by Christensen and Powers (2013), i.e., creating a simplified lithology column for each well based on the Vsh log and neutron-density, which were used to calibrate the GR log. As we are not able to show the Vsh log due to confidentially reasons, we have also calibrated our analysis with cutting samples. Along our depth range of interest, these samples were collected every 3 m, then washed on the drilling rig, with the lithologies averaged by the well site geologist (Figure 3). Our analysis combined data from all available wells, which include the two wells utilized by Torfstein and Steinberg (2020). At depths where >1 well penetrated the depth of interest, the logs and resulted lithologies were comparted, but besides slight bed-thickness variations, the interpreted lithologies are consistent between the wells.

Kinematic analysis was performed on 136 faults in the study area. The spatial and temporal evolution of the different structural elements, including the NW-SE-striking faults, were determined by following the methodology of Jackson et al. (2017): (1) depth-structure maps were used to highlight the current geometry of the sedimentary sequence. These maps were then used to generate thickness (isopach) maps that highlight the timing of syn-depositional structural activity: across-fault thickening indicates syn-sedimentary fault growth, and thinning across the Leviathan High indicates periods of syn-depositional folding (Thorsen, 1963; Jackson and Rotevatn, 2013; Jackson et al., 2017); (2) strike-parallel throw profiles (T-X) were used to visualise the spatial distribution of strain within the fault system (Walsh and Watterson, 1990; Peacock and Sanderson, 1991, 1996; Childs et al., 1995, 2019). By measuring the throw along a fault length (we measured throws every 250 m, regardless of the fault length), T-X profiles can help indicate kinematic interaction between and the linkage of faults within the system (Peacock and Sanderson, 1991, 1996; Dawers and Anders, 1995; Nicol et al., 2010; Jackson and Rotevatn, 2013; Childs et al., 2019). This analysis is specifically beneficial when the piano-key faults are compared to polygonal faults, as polygonal faults are thought to have a higher degree of fault interaction and linkage (i.e., the system is more mature) with depth (Cartwright, 2011); (3) dip-parallel throw profiles (T-Z) were used to understand the role dip-linkage and mechanical stratigraphy had on fault growth and ultimate geometry (Muraoka and Kamata, 1983; Peacock and Sanderson, 1991; Childs et al., 1996; Cartwright et al., 1998; Rykkelid and Fossen, 2002; Baudon and Cartwright, 2008b; Roche et al., 2012; Jackson and Rotevatn, 2013; Jackson et al., 2017; Rotevatn et al., 2019). T-Z plots also help us infer the depth and correlative geological period at which the faults nucleated (Barnett et al., 1987; Walsh and Watterson, 1988; Nicol et al., 1996a; Walsh et al., 2003; Jackson and Rotevatn, 2013; Wrona et al., 2017). We extracted T-Z plots from the position of maximum throw, as identified on the T-X plots. Similar techniques have been applied in previous studies to highlight how sandstone intervals separate polygonal fault tiers and how they are themselves characterised by a local minima (Lonergan et al., 1998; Stuevold et al., 2003; Cartwright, 2011;

Jackson et al., 2014; Ghalayini et al., 2017; Turrini et al., 2017; Wrona et al., 2017); (iv) expansion index (EI) plots (i.e., hangingwall vertical thickness of a stratigraphic package divided by its footwall vertical thickness) were constructed to identify growth strata and hence determine if faults breached the surface during their development (Jackson et al., 2017). Growth strata are highlighted where EI>1 (Thorsen, 1963; Cartwright et al., 1998; Tvedt et al., 2013; Robson et al., 2017). EI plots were constructed at the same sites where throw-depth plots were taken.

5. Results

Here we integrate our observations of seismic facies variability with drilling data to constrain the age and lithology of our new, sub-evaporite, seismic-stratigraphic framework. Thickness changes within different units are also highlighted, which help infer the timing and pattern of deformation. We then integrate this with our detailed analysis of the geometry and kinematics of the NW-SE-striking, layer-bound faults (sections 5.3 and 5.4), such that we can ultimately propose a mechanical model for fault development (Section 6).

5.1. Seismic-Stratigraphic Framework and Integration with Drilling Data

In addition to the base-evaporite horizon, we interpreted 10 pre-evaporite horizons to constrain the 10 seismic-stratigraphic units (Figure 1). Each section below begins with a description of the unit seismic facies and lithology, the latter derived from drilling data. Then, the current geometry of its bounding upper surface and if present, any thickness changes within the unit are also characterised. This structural framework provides the foundation for the kinematic analysis linking the timing of layer-bound faulting and other regional tectonic events in the Southern Levant Basin.

Unit 1: Pre-Conianian

Unit 1 is characterised by sub-horizontal, continuous, moderate-amplitude reflections and is capped by the bright, continuous, 'Upper Cretaceous Unconformity' horizon (Figure 2C). On the basis of published onshore and shallow offshore wells (i.e., no wells penetrated this unit in the deep-offshore), the Mid-Jurassic to Turonian (Mid Upper Cretaceous) unit comprises deep-water clastics, and pelagic and hemipelagic carbonates (Gardosh, Druckman, Buchbinder, and Rybakov, 2008; Gardosh et al., 2011). The top of unit 1 outline the large, triangular Leviathan High, which is located at the centre of the study area. The high is bounded to the north by an ENE-WSW-striking fault and to the south by a NE-striking, SE-dipping monocline (Figure

4A). No thickness analysis is presented for this unit as we did not have any lower boundary reflection to constrain this unit.

Unit 2: Coniacian - Eocene (33.9)

Unit 2 is characterised by chaotic, mostly transparent or low-amplitude seismic reflections and is capped by the bright, continuous, 'Eocene Unconformity' (33.9 Ma) (Figure 2). Our lithological analysis of X-1 well indicate that Unit 2 is composed of deep-water chalk and marls, which is in agreement with previous studies of the deep Levant Basin (Figure 3) (Gardosh, Druckman, Buchbinder, and Calvo, 2008; Steinberg et al., 2011; Gardosh and Tannenbaum, 2014). The Leviathan High is still well-expressed at the top of Unit 2, with NW-striking faults are also developed at this level (Figure 4B). Unit 2 (Figure 5A) thins across the Leviathan High and it gently thickens from the footwall to the hanging wall of the faults. The unit age corresponds to the same age as the Syrian Arc I, therefore the thickness changes seen here suggest an uplift/folding of the Leviathan High alongside fault activity during this time.

Unit 3: Rupelian – Early Chattian (33.9 – 24.07 Ma)

Characterised by sub-horizontal, semi-transparent, moderate amplitude seismic reflections, Unit 3 is capped by the bright, semi-continuous Intra-Chattian horizon (24.07 Ma) (Figure 2). The lithological analysis from X-1 well shows that this deep Oligocene unit is composed by thin (~5 m thick) sandstone beds within a mostly mudstone-dominated sequence (Figure 3). The Leviathan High is also well-expressed at the top of Unit 3, with the NW-striking faults also well developed (Figure 4C). Degradation in the imaging quality at this depth interval make the Intra-Chattian horizon difficult to map (Figure 4C), as expressed in the southern portion of the thickness map for Unit 3 (Figure 5B). However, it is still clear that Unit 3 is broadly tabular and of uniform thickness, indicating the main tectonic event(s) occurring during in Unit 2 had largely stopped (Figure 5B).

Unit 4: Late Chattian (24.07 – 23.02 Ma)

Unit 4 is characterised by a sub-horizontal, mostly continuous, moderate to high amplitude seismic facies, and is capped by the semi-continuous, moderate to low amplitude Top Oligocene horizon (23.02 Ma) (Figure 2). Like Unit 3, Unit 4 is composed by alternations of sandstone and mudstone (Figure 3). The top of Unit 4 still shows the Leviathan High and the NW-SE-striking faults (Figure 4D). As with Unit 3, Unit 4 is isopachous (Figure 5C).

Unit 5: Aquitanian (23.02 – 21.2 Ma)

Unit 5 is composed of sub-horizontal, continuous, moderate amplitude reflections that become stronger upwards, until reaching the bright, continuous, regionally extensive Top Aquitanian horizon (21.2 Ma) (Karcz et al., 2019) (Figure 2). Penetrated by five of the six wells, Unit 5 is also composed of alternating sandstone and mudstone, like Units 3 and 4 (Figure 3). The Leviathan High, the NW-SE-striking faults and the WNW-ENE-striking strike-slip faults are all very clearly expressed at the top Unit 5 map (Unit 4E). Like Unit 3 and 4 Unit 5 is broadly isopachous (Figure 5D).

Unit 6: Early Burdigalian (21.2 – 17.54 Ma)

Unit 6 is characterised by sub-horizontal, semi-continuous, moderate amplitude seismic reflections, capped by the moderate amplitude Intra-Burdigalian horizon (17.54 Ma) (Figure 2). Unit 6 is more sandstone-prone than the deeper units with Net-to-Gross of 70% (Karcz et al., 2019), and it contains the stratigraphically youngest sandstones present within the faulted units (Figure 3). Similar relatively high Net-to-Gross sandstone units are described in neighbouring fields (Christensen and Powers, 2013; Stearman et al., 2021; see their Figure 1). The high Net-to-Gross of this unit has substantial impact of the fault-growth model we present later in this manuscript (see section 6.1.2.). The top of Unit 6 continues to show the Leviathan High and the NW-SE-striking faults (Figure 4F). Unit 6 gently thins towards the WSW-ENE-striking strike-slip fault, but no thickness changes are seen across the faults (Figure 5E). This NW thinning trend towards the strike-slip fault may suggest a renewed tectonic activity in the study area.

Unit 7: Late Burdigalian – Middle Langhian (17.54 – 14.4 Ma)

Unlike the units below, Unit 7 is characterised by semi-transparent, low to medium amplitude seismic reflections, capped by the continuous, bright Intra Langhian horizon (14.4 Ma) (Figure 2). Unit 7 is mudstone-dominated and contains thin (<5 m thick) carbonate beds; sandstone is notably absent (Figure 3). Because the carbonate beds are relatively thin, they are not clearly detected in well-logs; however, they are observed in all six well-site analyses, documented in cutting samples and composite logs. In addition to the triangular Leviathan High and the NW-SE-striking faults, the Intra-Langhian structural map also shows a system of polygonally arranged depressions (Figure 6), which locally become concentric around the Tamar anticline (Figure 6C). Besides thickness changes associated with the NW-striking faults (Figure 7), Unit 7 also shows thinnings across the Leviathan High (Figure 5F), indicating significant tectonic activity period.

In detail, flattening the Top Langhian horizon reveals a significant intra-formational onlap horizon within Unit 7 (Figure 8). This horizon, which is dated as Late Burdigalian (~15 Ma), divides Unit 7 into two (Figure 8). The lower sub-unit 7 (7a) is broasdly tabular and seismic reflections are continuous over the Leviathan High (Figure 8C & E), whearas the upper sub-unit (7b) onplaps this Late Burdigalian horizon on both sides of the Leviathan High (Figure 8 C & D).

Unit 8: Late Langhian (14.4 – 13.82 Ma)

Unit 8 is characterised by sub-horizontal, continuous high amplitude seismic reflections, and is capped by a very high amplitude Top Langhian horizon (13.82 Ma) (Figure 2). Like Unit 7, Unit 8 is mudstone-dominated, containing thin (< 5 m thick) carbonate beds (Figure 3). The Leviathan High, and the polygonal fabric are well expressed on the top of Unit 8, while the NW-SE-striking faults are not as well expressed as in the deeper units (Figure 6). Like sub-Unit 7b, Unit 8 thins across the Leviathan High, with no faulting-related thickness changes, suggesting that faulting was no longer syn-depositional (Figure 5G).

We note that the top of Unit 8 defines an unconformity, with Serravallian strata missing in the two wells studied by Torfstein and Steinberg (2020). Those authors show that Unit 8 is capped by a mudstone-rich, carbonate-poor Tortonian unit (Unit 9), suggesting the top of the Langhian coincides with the global Miocene Carbonate Crash event, and concluding that the unconformity resulted from a large-scale carbonate dissolution event. This dissolution event may be responsible for the polygonal pattern identified in Unit 8. Stratigraphically, these depressions are confined to Unit 8, and are present *above* the growth strata associated with the NW-SE-striking, layer-bound faults (Unit 7), meaning their formation *and* deformation post-date at least the main, initial period of faulting. It is therefore possible that displacement of the polygonal fabric occurred due to subsequent upward propagation of the faults when the faults were not surface-breaking.

Unit 9: Early Tortonian (13.82 – 9.18 Ma)

Unit 9 is characterised by a chaotic, low-amplitude seismic-facies which is capped by a moderate amplitude, continuous Intra-Tortonian horizon (9.18 Ma) (Figure 2). Torfstein and Steinberg (2020) note that Unit 9 is mudstone-rich and foraminifera- and $CaCO_3$-poor, indicative of carbonate dissolution (see above). Because of its chaotic seismic signature, we cannot say for certain whether the faults extend through Unit 9, although the top of the unit does not appear to be deformed by these structures (Figure 4I). Unit 9 clearly thins across the

Leviathan High (Figure 5H) indicating the second tectonic activity which started at Unit 7 is continuous here. The origin of this chaotic section is beyond the scope of this manuscript, but we do suggest a possible correlation to similar observations made by Papamitriou et al. (2018), where they suggested a similar chaotic section on the flanks of the Eratosthenes Seamount, triggered by the collision between the Seamount and Cyprus.

Unit 10: Late Tortonian (9.18 – 5.96 Ma)

Unlike Unit 9, Unit 10 is characterised by sub-horizontal, continuous, moderate amplitude seismic reflections, capped by the base-evaporites bright and continuous seismic horizon (Figure 2). Unit 10 is lithologically similar to Unit 9, comprising foraminifera- and $CaCO_3$-poor mudstone (Torfstein and Steinberg, 2020). The top of Unit 10 dips gently north-westwards, although three large channels are present (Figure 4J). The NW-striking faults are absent. Similar to Unit 9, Unit 10 thins across the Leviathan High (Figure 5E).

In summary, our dataset is dominated by the large, triangular-shaped Leviathan High and numerous NW-SE-striking, layer-bound (i.e., by the Top Langhian and Base Oligocene horizons) normal faults. Thickness changes are seen in two main stratigraphic intervals and corresponding time periods: the first during the Coniacian - Eocene, where thinning across the Leviathan High is most dominant, and the second during the Burdigalian and Langhian, where marked thickness changes occur not only across the Leviathan High, but also across the NW-SE-striking faults. These two phases of deformation appear to have been separated by a period of relative quiescence.

5.2. Other Prominent Structural Elements

In addition to the NW-striking piano-key faults and the Leviathan High described above, a prominent ENE-WSW-striking fault exists across our study area along the northern edge of the Leviathan High. Cross-sections across the fault indicate that it corresponds with a deep, single stem which cross-cuts the entire Coniacian to Oligo-Miocene sedimentary sequence (Figure 9A). From its single stem, splays spread in a negative flower structure along the Top Aquitanian horizon (Figure 8A). Spectral decomposition along the Top Aquitanian horizons highlight this WSW-ENE-striking fault, which is composed of several, similarly striking, segments (Figure 9C). Adjacent to these segments, the otherwise NW-SE-striking piano-key faults change their strike to N-S, perpendicular and locally physically linked to the ENE-WSW-striking fault system (Figure 9C). Similar geometric relationship are seen in the adjacent Karish gas field (~50 km east of our study area). There, NW-striking faults abut against the 'Karish Shear Zone'

(Gouliotis, 2019), a WSW-ENE-striking, dextral strike-slip fault that could be the along-strike extension of the geometrically similarly fault found in our study area (Stearman et al., 2021). Additionally, we note two other smaller (~5 km long), ENE-WSW-striking faults at the centre of the study area, where the intensity of NW-striking faults is locally higher than elsewhere (Figure 9C&8E). Finally, in terms of their age, thickening of Units 7 and 8 indicates the ENE-WSW-striking structure was active in the Late Burdigalian to Late Langhian (Figure 7 & 9B).

Similar geometrical relationships between otherwise NW-SE-striking piano-key faults and WSW-ENE-striking faults are documented in the Northern Levant Basin (Ghalayini et al., 2014). There, the faults change their orientation to strike in an almost N-S direction and they are inferred to represent Riedel-like structures orientated at 60° from the dextral strike-slip fault (Ghalayini et al., 2014). The origin of these faults is not yet clear, but Ghalayini et al. (2014) suggested they may be related to a strike-slip reactivation of buried rift-related faults by the dextral movement along the Dead-Sea transform.

5.3. NW-SE-Striking Fault Geometry and Distribution

We have identified, mapped, and undertaken a geometric and kinematic analysis of 136, predominantly NW-SE-striking normal faults present within the Oligo-Miocene succession, bounded above by the Base Oligocene and below the Top Langhian (Figure 10). The faults have an average length of 6.3 km and average throw of 116 m (see section 5.4.2. for more details); and are normally displaced relative to their length (Figure 9B). Most faults (61%) dip to the SW, with seemingly no relationship between faults dip direction and their location, except to the north of the WSW-ENE-striking fault described above, where all the layer-bound faults dip SW (Figure 9A).

5.4. Kinematic Analysis of Layer-Bound Normal Faults

5.4.1. Throw-Length (T-X) analysis

Of the 136 mapped faults in the study area, 16 were not included in this analysis (or the T-Z analysis described below) because they extended outside of the seismic dataset and thus, we could not constrain their true length. Based on their throw vs. length profile shape, the faults were classified into four groups (TX1-4) (Figure 11). TX1 and TX2 are asymmetrical, with maximum throw offset to the SE or the NW, respectively, of the fault centre. TX3 are symmetrical, with maximum throw at the fault centre, whereas TX4 is defined by a profile containing two throw maxima (Figure 11). We do not see any direct spatial correlation between these groups and other structural elements; however, we do note that a change in the distribution of strain with depth. For example, our analysis shows that symmetrical profiles are more common with depth, i.e., whereas 37% of the faults displacing the upper boundary (Late Langhian horizon) have a symmetrical throw distribution, 67% of the faults displacing the lower boundary (Base Oligocene) have a symmetrical throw distribution (Figure 11). Given that symmetrical profiles typify less mature faults that have developed in kinematic isolation from surrounding structures, we infer a greater degree of fault interactions and higher fault maturity at shallower depth (Walsh and Watterson, 1990; Nicol et al., 2010).

5.4.2. Throw-Depth (T-Z) analysis

Throw-depth profiles were constructed for the same 120 faults analysed in sub-Section 5.4.1. Our analysis shows that the average T-Z profile is asymmetric, with maximum throw across the Intra-Burdigalian (17.54 Ma) horizon, decreasing upwards and downwards towards the fault tips (Figure 12A).

The faults were divided into two main groups based on their vertical extent (TZ1 and TZ2). TZ1 faults displace the entire Oligo-Miocene sequence, with an average length of 7.2 km, an average height of 1.9 km, and an average vertical throw of 128 m (Figure 12). TZ1 throw profiles are asymmetrical, with a prominent maximum throw along the Intra-Burdigalian horizon (Figure 12A). From this maximum, the throw profile decreases almost linearly both upwards to the base of the Lower Tortonian chaotic unit (Unit 9), and downwards to the Upper Chattian/Eocene units. TZ2 faults are smaller (average length of 4.2 km and a maximum throw of 80 m), their lower tip does not displace the Intra-Chattian horizon, and they exhibit a more symmetrical throw profile (Figure 12). Spatially, 70% of the mapped faults in the study area are TZ1, with TZ2 mostly located along the high's flanks (Figure 12C).

Compared to throw-depths plots by Ghalayini et al. (2017) and Ghalayini and Eid (2020) from the Northern Levant Basin offshore Lebanon, TZ1 faults are similar to their Type-1 faults and TZ2 are similar to their Type-3 faults (Figure 1 & 12). Whereas some similarities could be seen with regards to their throw-depth plots, the faults in the Northern and Southern Levant Basin do have their differences. Unlike Type-1 faults offshore Lebanon, TZ1 faults offshore Israel do not offset the base-Messinian evaporite, making them smaller than the Type-1 faults offshore Lebanon (height of 1.9 km vs 3.8 km), and with smaller vertical throw (120 m vs ~250 m). TZ2 and Type-3 faults do have very similar geometrical properties, but unlike Type-3 faults offshore Lebanon who are located along the basin margin (Figure 1), TZ2 faults are located in the deep basin (Figure 12).

5.4.3. Expansion Index

Expansion Index (EI) for the 120 faults analysed yielded EI>1 for Unit 7 (17.54 – 14.4 Ma) and Unit 8 (14.4 -13.82 Ma), with EI=1 for Unit 3 (33.9 – 24.07 Ma) (Figure 13A). Values < 1 is seen in the other units, possibly highlighting the difficulty associated with the interpretation of the bounding horizons (Figure 13A) (see further details in section 5.1). EI results strengthen our observations from sub-section 5.4.2., whereby all the faults, regardless of bottom tip depth, accumulated growth strata during the Late-Burdigalian, with possible continued activation during the Langhian (Figure 13B).

In summary, our thickness maps, seismic cross-sections, throw-depth profiles and expansion index data suggest that piano-key faults in the Southern Levant Basin breached the seabed during the Late Burdgialian. The correspondence between T_{max} position (inferred to represent the position of fault nucleation) and the base of the syn-kinematic sequence also implies the faults nucleated at or very near the seabed (see also Baudon & Cartwright, 2008a for a comparable example offshore Israel). Assessing the exact mechanics of near-seabed fault nucleation, which may be considered problematic given near-seabed sediments would be weakly unlithified and thus unable to sustain a shear fracture, is beyond the scope of this manuscript. However, it is possible that these faults nucleated at deeper depths, before rapidly attaining their final shape and size and breaching the seabed. as such, the faults may have rapidly transitioned from being blind to syn-depositional (see Baudon & Cartwright, 2008a).

6. Discussion

6.1. Mechanical model for the formation of the piano-key faults

We have shown that the non-polygonal, layer-bound faults identified in our study area breached the seabed during the Late Burdigalian. Regardless of their depth of nucleation the timing of faulting raises questions regarding their origin: (1) how can a diagenetic induced fault system, so strongly linked to very fine-grained sediments and sensitive to changes in host rock composition, propagate through a ~2 km thick sandstone prone host rock? (2) what occurred in the basin during the time of fault growth that caused their initial nucleation? (3) why are the faults so linear, striking NW-SE, perpendicular to the basin margin? To address these questions, we here describe possible mechanical models for their formation and discuss their implications.

6.1.1. Diagenetic model

Previous studies from the Northern Levant Basin, offshore Lebanon suggested that the piano-key faults nucleated and grew within mudstone-dominated host rock in accordance with the same diagenetic mechanism as the one typically associated with polygonal faults (Figure 1C) (Ghalayini et al., 2017; Ghalayini and Eid, 2020). Based on their relative geographic proximity, and the geometrical similarities between the piano-key faults in the Northern and Southern Levant Basins, we here test the role of such proposed diagenetic model in the latter.

Our lithological analysis shows the layer-bound faults in our study area had propagated through a ~2 km-thick sandstone-prone host rock. Sandstone-prone intervals of similar age are described in other neighbouring fields, suggesting that a relatively extensive, fan-like deep-water system was deposited in this part of the basin during the late-Miocene (Christensen and Powers, 2013; Gouliotis, 2019; Karcz et al., 2019; Stearman et al., 2021). At greater depths, only X-1 penetrated the faulted strata, an within this interval the seismic facies do not change away from the borehole. Regional studies also show that the Southern Levant basin experienced rapid sediment accumulation rates since the Oligocene. These coincide with incision events onshore Israel, and major progradation of the Nile Delta, suggesting that significant amounts of siliciclastic, sandstone-prone material reached the basin during the Oligocene and Early Miocene (Buchbinder et al., 1993; Gardosh et al., 2008; Steinberg et al., 2011; Gvirtzman et al., 2014; Torfstein and Steinberg, 2020). These local and regional observations all suggest that the Oligocene-Miocene sequence in the Southern Levant basin was sandstone-prone, challenging the application of the diagenetic model for the Southern Levant Basin layer-bound faults. Our interpretation is that nucleation and growth of these faults were unrelated to near-surface diagenesis of fine-grained sediments, as supported by our kinematic analysis.

T_{max} typically occurs along the Intra-Burdigalian for all fault types, suggesting that they nucleated along the Intra-Burdigalian horizon (17.54 Ma) (assuming the depth of maximum throw corresponds to the depth of fault nucleation; e.g., Nicol et al., 1996b; Kim and Sanderson, 2005). As the Intra-Burdigalian horizon also defines the base of the fault-related growth strata (i.e., Unit 7), we infer the faults nucleated as syn-depositional faults, displacing the seabed, during the Late Burdigalian. Thus, our throw-depth plots (e.g., Figure 12) and thickness maps (Figure 5) suggest the faults nucleated near their final upper tips, with significant down-dip propagation of their lower tips responsible for their vertical height.

We note that the T_{max} position described here differs to that characteristic of polygonal faults, where T_{max} (and the inferred site of fault nucleation) is located either at the centre or near the base of the fault surface (Cartwright, 2011; Wrona et al., 2017). This difference may reflect the contrasting origins and styles of growth of true polygonal faults and the layer-bound fault system described here. Specifically, the very fine-grained sediments must first be buried to activate the diagenetic processes, and thus nucleate polygonal faults. In contrast, based on the assumption that T_{max} represents the site of fault nucleation, the layer-bound faults studied here apparently nucleated as syn-depositional faults close to the seabed and propagated downwards (Cartwright, 2011; Seebeck et al., 2015) (Figure 11). Morgan et al. (2015) challenges this assumption, proposing that polygonal faults can nucleate at the lower parts of a tier, as buried faults, but due to mechanical constrains imposed by an underlying mechanical barrier, which inhibits downwards propagation of the fault basal tip, T_{max} can migrate upwards the tier centre. Even if this was the case in our layer-bound fault system, this would mean the faults still nucleated in a sandstone-prone units, challenging the link present between fault formation and the diagenesis of very fine-grained sediments (i.e., the diagenetic model). Moreover, nucleation of the faults in our study area (TZ2) do not reach the base of the tier, but instread stop at different depth within the tier in the absence of any apparent mechanical barrier. Therefore, based on their nucleation and propagation within a sandstone-prone unit and their atypical distribution of throw compered to “true” polygonal faults, we suggest that the layer-bound faults in our study area did not form in response to diagenesis of very fine-grained sediment, bringing us to an alternative, tectonic-related model (see Sub-Section 6.1.2.).

6.1.2. Tectonically induced layer-bound faulting

Given our arguments against a diagenetic model for fault development, we here present an alternative model that is summarised in Figure 14. Our model uses our age-constrained seismic-stratigraphic framework and refers to the tectono-stratigraphic events that shaped the basin during times of fault nucleation and subsequent growth.

First, we note that Unit 2 acts as a basal décollement layer for the layer-bound faults across not only the Southern Levant Basin, as demonstrated here, but across much of the eastern Mediterranean (Hawie et al., 2013; Ghalayini et al., 2014, 2017; Gao et al., 2020). To the best of our knowledge, X-1 is the only well in the basin to penetrate Unit 2. This well encountered Late Eocene strata but was aborted due to overpressure at that level. The exact reason for this overpressure is not known, but it is possible that the overpressure was developed by the rapidly buried Unit 2, leading to trapped fluids in the chalk and marls, eventually creating favourable conditions for overpressure to build. From a geodynamic perspective, compressional stresses associated with Syrian Arc folding, which were highest during the Coniacian - Eocene, are thought to have declined during the Oligocene (Sagy et al., 2018). This decrease in tectonic deformation is recorded in our study by a broadly isopachous, Early Oligocene unit (i.e., Unit 3) (Figure 5 and 14A). Rapid deposition continued throughout the Oligocene and Early Miocene (i.e., Units 4 and 5). This could therefore have caused pore pressure to build in the now-buried chalk and marls, driving disequilibrium compaction to the point of overpressure development in the impermeable unit, eventually leading to the formation of an intra-stratal décollement (Cosgrove, 2001; Jolly and Lonergan, 2002; Morley et al., 2008) (Figure 14 B&C).

Following this period of tectonic quiescence since Eocene, evidence for deformation appear again in the Burdigalian. Thinning of the sandstone-prone, Lower Burdigalian (Unit 6) towards the WSW-ENE-striking strike-slip fault, suggest this large fault was active at this time (Figure 5E). Initial activation of this strike-slip fault was followed by intense layer-bound faulting during the Late Burdigalian, in the mudstone-dominated Unit 7a (Figure 8E and 14D). By the end of the Langhian, both the strike-slip movement and the layer-bound normal faulting had stopped, while uplift of the Leviathan High became the most prominent deformation event (Figure 8D). The nucleation and subsequent growth of the faults prior to the culmination of any large-scale uplift, allows us to disregard the folding of the Leviathan High as a mechanism for the development of the normal faults.

We do note however, an apparent kinematic relationship between the WSW-ENE-striking strike-slip fault, and the layer-bound normal faulting, as both faulting systems were most active during the Late Burdigalian and had mostly ceased by the end of the Langhian. The origin of this strike-slip faulting is beyond the scope of this manuscript. However, we do highlight several significant geodynamic events that occurred in and around the basin during times of fault activation: (1) a landward jump of strain from the Continental Fault Zone along the Levant eastern margin, to the sinistral movement along the Dead Sea transform (Gvirtzman and Steinberg, 2012; Nuriel et al., 2017); (2) the development of the Dead Sea transform (Freund et al., 1968; Segev et al., 2014; Nuriel et al., 2017); (3) the final closure of the Indian Ocean-Mediterranean Seaway (Bialik et al., 2019; Torfstein and Steinberg, 2020); (4) change in the subduction rates and slab angle beneath the Cyprus Arc subduction zone (Gao et al., 2020; Aksu et al., 2021) (5) uplift of the Eratosthenes Seamount by >1 km at the Early Miocene (Robertson, 1998b; Papadimitriou et al., 2018; Gao et al., 2020)

A geodynamic outcome of these tectonic events may have been a counter-clockwise rotation of the basin, created by the non-subsiding Eratosthenes Seamount (Robertson, 2007; Papadimitriou et al., 2018; Aksu et al., 2021) (Figure 14E). As the Eratosthenes Seamount was stuck in place, the Levant Basin and its onshore segments, which continued to move northwards, rotated counter-clockwise around Eratosthenes. This counter-clockwise rotation could have therefore caused the formation of the offshore dextral strike-slip faults found in our dataset and offshore Lebanon (Figure 14E). A similar interpretation is made by Ghalayini et al. (2014), with these authors suggesting that continued sinistral movement along the Levant Fracture System onshore Lebanon caused (dextral) strike-slip reactivation of Cenozoic, rift-related normal fauls. They then propose that the relative movement along the strike-slip faults eventually created onshore counter-clockwise block rotation, absorbing any extension in the Levant Fracture System pull-up structures onshore Lebanon.

We here build on the model of Ghalayini et al. (2014) and propose that thick-skinned, dextral strike-slip movement along WSW-ENE-striking strike-slip faults occurred in response to the large-scale, geodynamic reorganisation of the Levant Basin. This strike-slip movement induced local extensional stresses and strain, with one expression of this being the NW-SE-striking, layer-bound normal faults (Figure 14). After nucleating, the NW-SE-striking faults propogated through the Oligocene-Miocene units until their lower tips decoupled within the overpressured Coniacian - Eocene unit. By introducing this tectonic-driven model we can explain: (1) the direct kinematic relationship we presented between the WSW-ENE-striking strike-slip fault and the NW-SE-striking faults; (2) the change in orientation from NW-SE-striking to a more E-W-striking, riedel-like orientation close to the strike-slip faults, as observed here and offshore Lebanon; (3) how the NW-SE-striking, layer-bound faults propogated through a ~ 2 km-thick sandstone-prone unit; (4) why the faults are so linear, and stike almost perpendicular to the current basin margin.

We do note that, unlike the Eocene, which is the lower boundary for the entire fault system across the Levant basin, the faults upper boundary varies; from the base-Evaporite (5.96 Ma) unit in the Northern Levant Basin, to the Top Langhian (13.84 Ma) at the Southern Levant Basin. We do not have clear explanation to this discrepancy. One possibility is that the strike-slip faults, and their kinematically related normal faults, remained active for longer in the Northern Levant Basin (Ghalayini et al., 2014). Another possibility for this discrepancy is the presence of the chaotic section in Unit 9 in our dataset, which is not present in the Northern

Levant Basin. It is therefore possible that upper fault propagation was inhibited by the more ductile nature of the chaotic section.

7. Conclusions

We use high-quality 3D seismic reflection, biostratigraphy, and well-log data to characterise the spatial and temporal evolution of a layer-bound fault system in the Southern Levant Basin, offshore Israel. We present a new, age-constrained, pre-Messinian seismic-stratigraphic framework for the basin, discussing the lithological variability and prominent thickness changes occurring within key intervals. This seismic-stratigraphic framework allows us to describe the prominent structural elements in our study area, which include the NW-striking, layer-bound faults, the triangular Leviathan High, and a prominent, WSW-striking, dextral strike-slip fault. Throw-depth profiles, expansion index, and thickness changes all indicate the layer-bound faults nucleated as syn-depositional faults during the Late Burdigalian (~15-17.54 Ma) in a mudstone-dominated unit. The faults then propagated downwards through sandstone-prone Oligocene-Miocene units, tipping-out within an overpressured Coniacian - Eocene strata. The NW-striking faults also appear to be kinematically linked to the WSW-striking strike-slip.

Based on: (1) their direct kinematic relations to the strike-slip fault; (2) their propagation through sandstone-prone strata; (3) throw-depth profiles which show maximum throw at the top of the faults, differing from other documented polygonal faults; and despite nucleating in a mudstone-dominated unit, we suggest the faults did not develop through a diagenetic process as previously suggested, but as a thin-skinned response to a thick-skinned tectonic reorganisation of the basin. The precise mechanics and kinematics of this geodynamic events are not clear, but they may relate to a possible counter-clockwise rotation of the basin, with spatially limited extension being accommodated by the layer-bound faults. This model suggests that basin-scale layer-bound normal faults can develop not only thought a diagenetic model as proposed for polygonal faults, but also by tectonic-related processes. Therefore, we suggest that linear, layer-bound normal fault system should be investigated in the context of the basin in which they formed in.

References

Aksu, A. E., J. Hall, and C. Yaltırak, 2021, Miocene–Quaternary tectonic, kinematic and sedimentary evolution of the eastern Mediterranean Sea: A regional synthesis: Earth-Science Reviews, v. 220, p. 103719, doi:https://doi.org/10.1016/j.earscirev.2021.103719.

Bar, O., Z. Gvirtzman, S. Feinstein, and E. Zilberman, 2013, Accelerated subsidence and sedimentation in the Levant Basin during the Late Tertiary and concurrent uplift of the Arabian platform: Tectonic versus counteracting sedimentary loading effects: Tectonics, v. 32, no. 3, p. 334–350, doi:10.1002/tect.20026.

Bar, O., E. Zilberman, S. Feinstein, R. Calvo, and Z. Gvirtzman, 2016, The uplift history of the Arabian Plateau as inferred from geomorphologic analysis of its northwestern edge: Tectonophysics, v. 671, p. 9–23, doi:10.1016/j.tecto.2016.01.004.

Barnett, J. A. M., J. Mortimer, J. H. Rippon, J. J. Walsh, and J. Watterson, 1987, Displacement Geometry in the Volume Containing a Single Normal Fault1: AAPG Bulletin, v. 71, no. 8, p. 925–937, doi:10.1306/948878ED-1704-11D7-8645000102C1865D.

Baudon, C., and J. Cartwright, 2008a, Early stage evolution of growth faults: 3D seismic insights from the Levant Basin, Eastern Mediterranean: Journal of Structural Geology, v. 30, no. 7, p. 888–898, doi:10.1016/j.jsg.2008.02.019.

Baudon, C., and J. Cartwright, 2008b, The kinematics of reactivation of normal faults using high resolution throw mapping: Journal of Structural Geology, v. 30, no. 8, p. 1072–1084, doi:10.1016/j.jsg.2008.04.008.

Ben-Gai, Y., 2018, The Leviathan Miocene Diapir – A novel insight into the tectonic evolution of the Southern Levant Basin, Eastern Mediterranean: Marine and Petroleum Geology, v. 89, p. 701–713, doi:10.1016/j.marpetgeo.2017.11.002.

Bialik, O. M., M. Frank, C. Betzler, R. Zammit, and N. D. Waldmann, 2019, Two-step closure of the Miocene Indian Ocean Gateway to the Mediterranean: Scientific Reports, v. 9, no. 1, p. 1–10, doi:10.1038/s41598-019-45308-7.

Bosworth, W., P. Huchon, and K. McClay, 2005, The Red Sea and Gulf of Aden Basins: Journal of African Earth Sciences, v. 43, no. 1, p. 334–378, doi:https://doi.org/10.1016/j.jafrearsci.2005.07.020.

Bosworth, W., D. F. Stockli, and D. E. Helgeson, 2015, Integrated outcrop, 3D seismic, and geochronologic interpretation of Red Sea dike-related deformation in the Western Desert, Egypt – The role of the 23Ma Cairo “mini-plume”: Journal of African Earth Sciences, v. 109, p. 107–119, doi:https://doi.org/10.1016/j.jafrearsci.2015.05.005.

Buchbinder, B., G. M. Martinotti, R. Siman-Tov, and E. Zilberman, 1993, Temporal and spatial relationships in Miocene reef carbonates in Israel: Palaeogeography, Palaeoclimatology, Palaeoecology, v. 101, no. 1, p. 97–116, doi:https://doi.org/10.1016/0031-0182(93)90154-B.

Carruthers, D., J. Cartwright, M. P. A. Jackson, and P. Schutjens, 2013, Origin and timing of layer-bound radial faulting around north sea salt stocks: New insights into the evolving stress state around rising diapirs: Marine and Petroleum Geology, v. 48, p. 130–148, doi:10.1016/j.marpetgeo.2013.08.001.

Cartwright, J., 2011, Diagenetically induced shear failure of fine-grained sediments and the development of polygonal fault systems: Marine and Petroleum Geology, v. 28, no. 9, p. 1593–1610, doi:10.1016/J.MARPETGEO.2011.06.004.

Cartwright, J., R. Bouroullec, D. James, and H. Johnson, 1998, Polycyclic motion history of some Gulf Coast growth faults from high-resolution displacement analysis: Geology, v. 26, no. 9, p. 819–822, doi:10.1130/0091-7613(1998)026<0819:PMHOSG>2.3.CO;2.

Cartwright, J. A., and D. N. Dewhurst, 1998, Layer-bound compaction faults in fine-grained sediments: GSA Bulletin, v. 110, no. 10, p. 1242–1257, doi:10.1130/0016-7606(1998)110<1242:lbcfif>2.3.co;2.

Cartwright, J., D. James, and A. Bolton, 2003, The genesis of polygonal fault systems: A review: Geological Society Special Publication, v. 216, p. 223–234, doi:10.1144/GSL.SP.2003.216.01.15.

Cartwright, J. A., and L. Lonergan, 1996, Volumetric contraction during the compaction of mudrocks: a mechanism for the development of regional-scale polygonal fault systems: Basin Research, v. 8, no. 2, p. 183–193, doi:10.1046/j.1365-2117.1996.01536.x.

Childs, C., A. Nicol, J. J. Walsh, and J. Watterson, 1996, Growth of vertically segmented normal faults: Journal of Structural Geology, v. 18, no. 12, p. 1389–1397, doi:10.1016/S0191-8141(96)00060-0.

Childs, C., J. Watterson, and J. J. Walsh, 1995, Fault overlap zones within developing normal fault systems: Journal of the Geological Society, v. 152, no. 3, p. 535 LP – 549, doi:10.1144/gsjgs.152.3.0535.

Childs, C., R. P. Worthington, J. J. Walsh, and V. Roche, 2019, Conjugate relay zones: geometry of displacement transfer between opposed-dipping normal faults: Journal of Structural Geology, v. 118, p. 377–390, doi:https://doi.org/10.1016/j.jsg.2018.11.007.

Christensen, C. J., and G. Powers, 2013, Formation Evaluation Challenges In Tamar Field, Offshore Israel, in SPWLA 54th Annual Logging Symposium: p. 1–12.

Cohen, Z., V. Kaptsan, and A. Flexer, 1990, The Tectonic Mosiac of the Southern Levant: implications for Hydrocarbon Prospects: Journal of Petroleum Geology, v. 13, no. 4, p. 437–462, doi:10.1111/j.1747-5457.1990.tb00858.x.

Cosgrove, J. W. (2001). Hydraulic Fracturing During the Formation and Deformation of a Basin: A Factor in the Dewatering of Low-Permeability Sediments. AAPG Bulletin, 85(4), 737–748. https://doi.org/10.1306/8626C997-173B-11D7-8645000102C1865D

Craik, D., and Y. Ben-Gai, 2019, Syn-Tectonic Sedimentation Over a Miocene Gas-Bearing Structure-Sequence Stratigraphy Case Study of the Aphrodite Field, Levant Basin*: Search and Discovery, doi:10.1306/20464Craik2019.

Dawers, N. H., and M. H. Anders, 1995, Displacement-length scaling and fault linkage: Journal of Structural Geology, v. 17, no. 5, p. 607–614, doi:https://doi.org/10.1016/0191-8141(94)00091-D.

Dewhurst, D. N., J. A. Cartwright, and L. Lonergan, 1999, The development of polygonal fault systems by syneresis of colloidal sediments: Marine and Petroleum Geology, v. 16, no. 8, p. 793–810, doi:10.1016/S0264-8172(99)00035-5.

Druckman, Y., 1994, Subsurface geology and structural evolution of the northwestern Negev, southern Israel: Geological Survey of Israel.

Eckersley, A. J., J. Lowell, and P. Szafian, 2018, High-definition frequency decomposition: Geophysical Prospecting, v. 66, no. 6, p. 1138–1143, doi:https://doi.org/10.1111/1365-2478.12642.

Eyal, Y., 1996, Stress field fluctuations along the Dead Sea rift since the middle Miocene: Tectonics, v. 15, no. 1, p. 157–170, doi:10.1029/95TC02619.

Faccenna, C., P. Glišović, A. Forte, T. W. Becker, E. Garzanti, A. Sembroni, and Z. Gvirtzman, 2019, Role of dynamic topography in sustaining the Nile River over 30 million years: Nature Geoscience, v. 12, no. 12, p. 1012–1017, doi:10.1038/s41561-019-0472-x.

Freund, R., 1975, The Triassic-Jurassic structure of Israel and its relation to the origin of the eastern Mediterranean: Geological Survey of Israel.

Freund, R., I. Zak, and Z. W. I. Garfunkel, 1968, Age and rate of the sinistral movement along the Dead Sea Rift: Nature, v. 220, no. 5164, p. 253–255.

Gao, H., Z. Wen, B. Shi, Z. Wang, and C. Song, 2020, Tectonic characteristics of the t and its periphery: Implications for evolution of the eastern Mediterranean: Marine Geology, v. 428, p. 106266, doi:https://doi.org/10.1016/j.margeo.2020.106266.

Gardosh, M. A., and Y. Druckman, 2006, Seismic stratigraphy, structure and tectonic evolution of the Levantine Basin, offshore Israel: Geological Society Special Publication, v. 260, no. 1, p. 201–227, doi:10.1144/GSL.SP.2006.260.01.09.

Gardosh, M., Y. Druckman, B. Buchbinder, and R. Calvo, 2008, The Oligo-Miocene deepwater system of the Levant Basin: Geological Survey of Israel, 73 p., doi:GSI/33/2008.

Gardosh, M., Y. Druckman, B. Buchbinder, and M. Rybakov, 2008, The Levant Basin Offshore Israel: Stratigraphy, Structure, Tectonic Evolution and Implications for Hydrocarbon Exploration - revised edition. Geological Survey of Israel report GSI/4/2008: Geological Survey of Israel, 121 p.

Gardosh, M., Z. Garfunkel, Y. Druckman, and B. Buchbinder, 2010, Tethyan rifting in the Levant Region and its role in Early Mesozoic crustal evolution: Geological Society, London, Special Publications, v. 341, no. 1, p. 9 LP – 36, doi:10.1144/SP341.2.

Gardosh, M. A., and E. Tannenbaum, 2014, The Petroleum Systems of Israel, in Memoir 106: Petroleum Systems of the Tethyan Region: AAPG Special Volumes, p. 179–216, doi:10.1306/13431857m106298.

Gardosh, M., P. Weimer, and A. Flexer, 2011, The sequence stratigraphy of Mesozoic successions in the Levant margin, southwestern Israel: A model for the evolution of southern Tethys margins: AAPG Bulletin, v. 95, no. 10, p. 1763–1794, doi:10.1306/02081109135.

Garfunkel, Z., 1998, Constrains on the origin and history of the Eastern Mediterranean basin: Tectonophysics, v. 298, no. 1–3, p. 5–35, doi:10.1016/S0040-1951(98)00176-0.

Garfunkel, Z., 1981, Internal structure of the Dead Sea leaky transform (rift) in relation to plate kinematics: Tectonophysics, v. 80, no. 1–4, p. 81–108, doi:10.1016/0040-1951(81)90143-8.

Garfunkel, Z., 2004, Origin of the Eastern Mediterranean basin: A reevaluation: Tectonophysics, v. 391, no. 1- 4 SPEC.ISS., p. 11–34, doi:10.1016/j.tecto.2004.07.006.

Garfunkel, Z., 1997, The history and formation of the Dead Sea basin, in T. M. Niemi, Z. Ben-Avraham, and J. R. Gat, eds., The Dead Sea, the Lake and its Setting: Oxford University Press, USA, p. 36–56.

Garfunkel, Z., and B. Derin, 1984, Permian-early Mesozoic tectonism and continental margin formation in Israel and its implications for the history of the Eastern Mediterranean: Geological Society Special Publication, v. 17, no. 1, p. 187–201, doi:10.1144/GSL.SP.1984.017.01.12.

Ghalayini, R., J.-M. Daniel, C. Homberg, F. H. Nader, and J. E. Comstock, 2014, Impact of Cenozoic strike-slip tectonics on the evolution of the northern Levant Basin (offshore Lebanon): Tectonics, v. 33, no. 11, p. 2121–2142, doi:10.1002/2014TC003574.

Ghalayini, R., and C. Eid, 2020, Using polygonal layer-bound faults as tools to delimit clastic reservoirs in the Levant Basin offshore Lebanon: AAPG Bulletin, v. 104, no. 3, p. 629–656, doi:10.1306/07151918155.

Ghalayini, R., C. Homberg, J. M. Daniel, and F. H. Nader, 2017, Growth of layer-bound normal faults under a regional anisotropic stress field: Geological Society, London, Special Publications, v. 439, no. 1, p. 57 LP – 78, doi:10.1144/SP439.13.

Gouliotis, L., 2019, Tectonic Structure of the Karish Gas Field, Offshore Israel Tectonics and Hydrogeology of Sterea Hellas View project Researches on the geology of Greece View project: Search and Discovery, no. 30638, doi:10.1306/30638Gouliotis2019.

Goulty, N. R., 2008, Geomechanics of polygonal fault systems: A review: p. 389–397, doi:10.1144/1354-079308-781.

Goulty, N. R., 2002, Mechanics of layer-bound polygonal faulting in fine-grained sediments: Journal of the Geological Society, v. 159, no. 3, p. 239–246, doi:10.1144/0016-764901-111.

Granot, R., 2016, Palaeozoic oceanic crust preserved beneath the eastern Mediterranean: Nature Geoscience, v. 9, no. 9, p. 701–705, doi:10.1038/ngeo2784.

Gvirtzman, Z., I. Csato, and D. Granjeon, 2014, Constraining sediment transport to deep marine basins through submarine channels: The Levant margin in the Late Cenozoic: Marine Geology, v. 347, p. 12–26, doi:10.1016/j.margeo.2013.10.010.

Gvirtzman, Z., M. Reshef, O. Buch-Leviatan, G. Groves-Gidney, Z. Karcz, Y. Makovsky, and Z. Ben-Avraham, 2015, Bathymetry of the Levant basin: Interaction of salt-tectonics and surficial mass movements: Marine Geology, v. 360, p. 25–39, doi:10.1016/j.margeo.2014.12.001.

Gvirtzman, Z., and J. Steinberg, 2012, Inland jump of the Arabian northwest plate boundary from the Levant continental margin to the Dead Sea Transform: Tectonics, v. 31, no. 4, p. n/a-n/a, doi:10.1029/2011TC002994.

Gvirtzman, Z., J. Steinberg, O. Bar, B. Buchbinder, E. Zilberman, R. Siman-Tov, R. Calvo, L. Grossowicz, A. Almogi-Labin, and M. Rosensaft, 2011, Retreating late tertiary shorelines in Israel: Implications for the exposure of north Arabia and levant during Neotethys closure: Lithosphere, v. 3, no. 2, p. 95–109, doi:10.1130/L124.1.

Hawie, N., C. Gorini, R. Deschamps, F. H. Nader, L. Montadert, D. Granjeon, and F. Baudin, 2013, Tectono-stratigraphic evolution of the northern Levant Basin (offshore Lebanon): Marine and Petroleum Geology, v. 48, p. 392–410, doi:10.1016/j.marpetgeo.2013.08.004.

Hsü, K. J., L. Montadert, D. Bernoulli, M. B. Cita, A. Erickson, R. E. Garrison, R. B. Kidd, F. Mèlierés, C. Müller, and R. Wright, 1977, History of the mediterranean salinity crisis: Nature, v. 267, no. 5610, p. 399–403, doi:10.1038/267399a0.

Ireland, M. T., N. R. Goulty, and R. J. Davies, 2011, Influence of stratigraphic setting and simple shear on layer-bound compaction faults offshore Mauritania: Journal of Structural Geology, v. 33, no. 4, p. 487–499, doi:10.1016/j.jsg.2010.11.005.

Jackson, C. A. L., R. E. Bell, A. Rotevatn, and A. B. M. Tvedt, 2017, Techniques to determine the kinematics of synsedimentary normal faults and implications for fault growth models: Geological Society Special Publication, v. 439, no. 1, p. 187–217, doi:10.1144/SP439.22.

Jackson, C. A. L., D. T. Carruthers, S. N. Mahlo, and O. Briggs, 2014, Can polygonal faults help locate deep-water reservoirs? AAPG Bulletin, v. 98, no. 9, p. 1717–1738, doi:10.1306/03131413104.

Jackson, C. A. L., and A. Rotevatn, 2013, 3D seismic analysis of the structure and evolution of a salt-influenced normal fault zone: A test of competing fault growth models: Journal of Structural Geology, v. 54, p. 215–234, doi:10.1016/j.jsg.2013.06.012.

Jolly, R. J. H., & Lonergan, L. (2002). Mechanisms and controls on the formation of sand intrusions. Journal of the Geological Society, 159(5), 605. https://doi.org/10.1144/0016-764902-025

Kanari, M., G. Tibor, J. K. Hall, T. Ketter, G. Lang, and U. Schattner, 2020, Sediment transport mechanisms revealed by quantitative analyses of seafloor morphology: New evidence from multibeam bathymetry of the Israel exclusive economic zone: Marine and Petroleum Geology, v. 114, p. 104224, doi:10.1016/j.marpetgeo.2020.104224.

Karcz, K., Y. Gellman, O. Shitrit, and J. Steinberg, 2019, The Leviathan Field - Nine Years Since Discovery and Nearing First Gas, in Second EAGE Eastern Mediterranean Workshop: European Association of Geoscientists & Engineers, p. 1–5, doi:10.3997/2214-4609.201903152.

Kim, Y. S., and D. J. Sanderson, 2005, The relationship between displacement and length of faults: A review: Earth-Science Reviews, v. 68, no. 3–4, p. 317–334, doi:10.1016/j.earscirev.2004.06.003.

King, J. J., and J. Cartwright, 2020, Ultra-slow throw rates of polygonal fault systems: Geological Society of America | GEOLOGY, v. 48, p. 473–477, doi:10.1130/G47221.1.

Kosi, W., G. Tari, F. H. Nader, C. Skiple, B. Trudgill, and D. Lazar, 2012, Structural analogy between the “piano key faults” of deep-water Lebanon and the extensional faults of the Canyonlands grabens, Utah, United States: The Leading Edge, v. 31, no. 7, p. 824–830, doi:10.1190/tle31070824.1.

Krenkel, E., 1924, Der Syrische Bogen: Zentralblatt Mineralogie, v. 9, no. 10, p. 274–281.

Krijgsman, W., F. J. Hilgen, I. Raffi, F. J. Sierro, and D. S. Wilson, 1999, Chronology, causes and progression of the Messinian salinity crisis: Nature, v. 400, no. 6745, p. 652–655, doi:10.1038/23231.

Lathrop, B., C. A. L. Jackson, and A. Rotevatn, n.d., Normal Fault Database_Lathrop.xlsx: <https://figshare.com/articles/dataset/Normal_Fault_Database_Lathrop_xlsx/17087273> (accessed February 23, 2022).

Lonergan, L., J. Cartwright, and R. Jolly, 1998, The geometry of polygonal fault systems in Tertiary mudrocks of the North Sea: Journal of Structural Geology, v. 20, no. 5, p. 529–548, doi:10.1016/S0191-8141(97)00113-2.

Morag, N., I. Haviv, and Y. Katzir, 2016, From ocean depths to mountain tops: Uplift of the Troodos ophiolite (Cyprus) constrained by low-temperature thermochronology and geomorphic analysis: Tectonics, v. 35, no. 3, p. 622–637, doi:10.1002/2015TC004069.

Morgan, D. A., J. A. Cartwright, and P. Imbert, 2015, Perturbation of polygonal fault propagation by buried pockmarks andthe implications for the development of polygonal fault systems: Marine and Petroleum Geology, v. 65, p. 157–171, doi:10.1016/j.marpetgeo.2015.03.024.

Morley, C. K., Tingay, M., Hillis, R., & King, R. (2008). Relationship between structural style, overpressures, and modern stress, Baram Delta Province, northwest Borneo. Journal of Geophysical Research: Solid Earth, 113(B9). https://doi.org/https://doi.org/10.1029/2007JB005324

Muraoka, H., and H. Kamata, 1983, Displacement distribution along minor fault traces: Journal of Structural Geology, v. 5, no. 5, p. 483–495, doi:10.1016/0191-8141(83)90054-8.

Needham, D. L., H. S. Pettingill, C. J. Christensen, J. Ffrench, and Z. K. Karcz, 2017, The Tamar giant gas field: Opening the Subsalt Miocene gas play in the Levant Basin, *in* AAPG Memoir: American Association of Petroleum Geologists, p. 221–256, doi:10.1306/13572009M1133688.

Nicol, A., J. J. Walsh, P. Villamor, H. Seebeck, and K. R. Berryman, 2010, Normal fault interactions, paleoearthquakes and growth in an active rift: Journal of Structural Geology, v. 32, no. 8, p. 1101–1113, doi:https://doi.org/10.1016/j.jsg.2010.06.018.

Nicol, A., J. Watterson, J. J. Walsh, and C. Childs, 1996a, The shapes, major axis orientations and displacement patterns of fault surfaces: Journal of Structural Geology, v. 18, no. 2, p. 235–248, doi:https://doi.org/10.1016/S0191-8141(96)80047-2.

Nicol, A., J. Watterson, J. J. Walsh, and C. Childs, 1996b, The shapes, major axis orientations and displacement patterns of fault surfaces: Journal of Structural Geology, v. 18, no. 2, p. 235–248, doi:https://doi.org/10.1016/S0191-8141(96)80047-2.

Nuriel, P., R. Weinberger, A. R. C. Kylander-Clark, B. R. Hacker, and J. P. Craddock, 2017, The onset of the Dead Sea transform based on calcite age-strain analyses: Geology, v. 45, no. 7, p. 587–590, doi:10.1130/G38903.1.

Ortega, J., R. Hebert, and Y. Gellman, 2019, The Dynamic Tamar Reservoir: Insights from Five Years of Production*: Search and Discovery, doi:10.1306/20465Ortega2019.

Othman, A. A. A., Fathy, M., & Maher, A. (2016). Use of spectral decomposition technique for delineation of channels at Solar gas discovery, offshore West Nile Delta, Egypt. *Egyptian Journal of Petroleum*, *25*(1), 45–51. https://doi.org/https://doi.org/10.1016/j.ejpe.2015.03.005

Papadimitriou, N., C. Gorini, F. H. Nader, R. Deschamps, V. Symeou, and J. C. Lecomte, 2018, Tectono-stratigraphic evolution of the western margin of the Levant Basin (offshore Cyprus): Marine and Petroleum Geology, v. 91, p. 683–705, doi:10.1016/j.marpetgeo.2018.02.006.

Peacock, D. C. P., and D. J. Sanderson, 1991, Displacements, segment linkage and relay ramps in normal fault zones: Journal of Structural Geology, v. 13, no. 6, p. 721–733, doi:https://doi.org/10.1016/0191-8141(91)90033-F.

Peacock, D. C. P., and D. J. Sanderson, 1996, Effects of propagation rate on displacement variations along faults: Journal of Structural Geology, v. 18, no. 2–3, p. 311–320, doi:10.1016/S0191-8141(96)80052-6.

Reiche, S., C. Hübscher, and M. Beitz, 2014, Fault-controlled evaporite deformation in the Levant Basin, Eastern Mediterranean: Marine Geology, v. 354, p. 53–68, doi:10.1016/j.margeo.2014.05.002.

Rider, M. H., & Kennedy, M. (2014). The Geological Interpretation of Well Logs. In *Rider-French Consulting Ltd*. Rider-French Consulting Limited.

Roberts, D. T., Crook, A. J. L., Cartwright, J. A., & Profit, M. L. (2015). Investigating the evolution of polygonal fault systems using geomechanical forward modeling. In 49th US Rock Mechanics / Geomechanics Symposium 2015 Vol. 1 (pp. 465-477)

Robertson, A., 1998a, Mesozoic-Tertiary tectonic evolution of the easternmost Mediterranean area: Integration of marine and land evidence: Proceedings of the Ocean Drilling Program: Scientific Results, v. 160, p. 723–784, doi:10.2973/odp.proc.sr.160.061.1998.

Robertson, A., 2007, Overview of tectonic settings related to the rifting and opening of Mesozoic ocean basins in the Eastern Tethys: Oman, Himalayas and Eastern Mediterranean regions: Geological Society of London, p. 325–388, doi:10.1144/SP282.15.

Robertson, A., 1998b, Tectonic significance of the Eratosthenes Seamount: a continental fragment in the process of collision with a subduction zone in the eastern Mediterranean (Ocean Drilling Program Leg 160): Tectonophysics, v. 298, no. 1, p. 63–82, doi:https://doi.org/10.1016/S0040-1951(98)00178-4.

Robson, A. G., R. C. King, and S. P. Holford, 2017, Structural evolution of a gravitationally detached normal fault array: analysis of 3D seismic data from the Ceduna Sub-Basin, Great Australian Bight: Basin Research, v. 29, no. 5, p. 605–624, doi:https://doi.org/10.1111/bre.12191.

Roche, V., C. Homberg, and M. Rocher, 2012, Fault displacement profiles in multilayer systems: From fault restriction to fault propagation: Terra Nova, v. 24, no. 6, p. 499–504, doi:10.1111/j.1365-3121.2012.01088.x.

Rotevatn, A., C. A. L. Jackson, A. B. M. Tvedt, R. E. Bell, and I. Blækkan, 2019, How do normal faults grow? Journal of Structural Geology, v. 125, p. 174–184, doi:10.1016/j.jsg.2018.08.005.

Ryan, W. B. F., 2009, Decoding the mediterranean salinity crisis: Sedimentology, v. 56, no. 1, p. 95–136, doi:10.1111/j.1365-3091.2008.01031.x.

Rykkelid, E., and H. Fossen, 2002, Layer rotation around vertical fault overlap zones: observations from seismic data, field examples, and physical experiments: Marine and Petroleum Geology, v. 19, no. 2, p. 181–192, doi:https://doi.org/10.1016/S0264-8172(02)00007-7.

Sagy, Y., Z. Gvirtzman, and M. Reshef, 2018, 80 m.y. of folding migration: New perspective on the Syrian arc from Levant Basin analysis: Geology, v. 46, no. 2, p. 175–178, doi:10.1130/G39654.1.

Sagy, Y., Z. Gvirtzman, M. Reshef, and Y. Makovsky, 2015, The enigma of the Jonah high in the middle of the Levant basin and its significance to the history of rifting: Tectonophysics, v. 665, p. 186–198, doi:10.1016/j.tecto.2015.09.037.

Seebeck, H., E. Tenthorey, C. Consoli, and A. Nicol, 2015, Polygonal faulting and seal integrity in the Bonaparte Basin, Australia: Marine and Petroleum Geology, v. 60, p. 120–135, doi:10.1016/j.marpetgeo.2014.10.012.

Segev, A., V. Lyakhovsky, and R. Weinberger, 2014, Continental transform-rift interaction adjacent to a continental margin: The Levant case study: Elsevier, p. 83–103, doi:10.1016/j.earscirev.2014.08.015.

Stearman, M., B. Gergurich, T. Kent, A. Wickard, and F. Laugier, 2021, Miocene Deep-Water Stratigraphic Architecture and Heterogeneity: Levant Basin, Offshore Cyprus and Israel, *in* Third EAGE Eastern Mediterranean Workshop: European Association of Geoscientists & Engineers, p. 1–3, doi:10.3997/2214-4609.202137034.

Steinberg, J., Z. Gvirtzman, Y. Folkman, and Z. Garfunkel, 2011, Origin and nature of the rapid late Tertiary filling of the Levant Basin: Geology, v. 39, no. 4, p. 355–358, doi:10.1130/G31615.1.

Steinberg, J., A. M. Roberts, N. J. Kusznir, K. Schafer, and Z. Karcz, 2018, Crustal structure and post-rift evolution of the Levant Basin: Marine and Petroleum Geology, v. 96, p. 522–543, doi:10.1016/j.marpetgeo.2018.05.006.

Stuevold, L. M., R. B. Faerseth, L. Arnesen, J. Cartwright, and N. Möller, 2003, Polygonal faults in the Ormen Lange Field, Møre Basin, offshore Mid Norway: Geological Society, London, Special Publications, v. 216, no. 1, p. 263 LP – 281, doi:10.1144/GSL.SP.2003.216.01.17.

Thorsen, C. E., 1963, Age of growth faulting in the southern Louisiana.: Gulf coast association of geological societies, v. 13, p. 103–110.

Torfstein, A., and J. Steinberg, 2020, The Oligo–Miocene closure of the Tethys Ocean and evolution of the proto-Mediterranean Sea: Scientific Reports, v. 10, no. 1, p. 13817, doi:10.1038/s41598-020-70652-4.

Turrini, L., C. A.-L. Jackson, and P. Thompson, 2017, Seal rock deformation by polygonal faulting, offshore Uruguay: Marine and Petroleum Geology, v. 86, p. 892–907, doi:10.1016/j.marpetgeo.2017.06.038.

Tvedt, A. B. M., A. Rotevatn, C. A.-L. Jackson, H. Fossen, and R. L. Gawthorpe, 2013, Growth of normal faults in multilayer sequences: A 3D seismic case study from the Egersund Basin, Norwegian North Sea: Journal of Structural Geology, v. 55, p. 1–20, doi:https://doi.org/10.1016/j.jsg.2013.08.002.

Walley, C. D., 1998, Some outstanding issues in the geology of Lebanon and their importance in the tectonic evolution of the Levantine region: Tectonophysics, v. 298, no. 1–3, p. 37–62, doi:10.1016/S0040-1951(98)00177-2.

Walsh, J. J., W. R. Bailey, C. Childs, A. Nicol, and C. G. Bonson, 2003, Formation of segmented normal faults: a 3-D perspective: Journal of Structural Geology, v. 25, no. 8, p. 1251–1262, doi:https://doi.org/10.1016/S0191-8141(02)00161-X.

Walsh, J. J., and J. Watterson, 1988, Analysis of the relationship between displacements and dimensions of faults: Journal of Structural Geology, v. 10, no. 3, p. 239–247, doi:10.1016/0191-8141(88)90057-0.

Walsh, J. J., and J. Watterson, 1990, New methods of fault projection for coalmine planning: Proceedings of the Yorkshire Geological Society, v. 48, no. 2, p. 209 LP – 219, doi:10.1144/pygs.48.2.209.

Wrona, T., C. Magee, C. A.-L. Jackson, M. Huuse, and K. G. Taylor, 2017, Kinematics of Polygonal Fault Systems: Observations from the Northern North Sea: p. 101.

Zachos, J., M. Pagani, L. Sloan, E. Thomas, and K. Billups, 2001, Trends, Rhythms, and Aberrations in Global Climate 65 Ma to Present: Science, v. 292, no. 5517, p. 686 LP – 693, doi:10.1126/science.1059412.

Ziegler, A. M., 2001, Late Permian to Holocene Paleofacies Evolution of the Arabian Plate and its Hydrocarbon Occurrences: GeoArabia, v. 6, no. 3, p. 445–504.

Zucker, E., Z. Gvirtzman, J. Steinberg, and Y. Enzel, 2019, Salt tectonics in the Eastern Mediterranean Sea: Where a giant delta meets a salt giant: Geology, v. 48, no. 2, p. 134–138, doi:10.1130/g47031.1.

Figure Captions

Figure 1: (A) A regional map of the Levant basin. Zoomed area shows the Ghalayini and Eid, (2020) published fault system offshore Lebanon and the three different fault types described by them. (B) Throw-depth profiles of these three fault types described offshore Lebanon (Modified from Ghalayini and Eid, 2020). (C) The diagenetically induced mechanical model suggested by Ghalayini and Eid, (2020) for offshore Lebanon (A-C are modified from Ghalayini and Eid, 2020).

Figure 2: (A) The location of the study area in the southern Levant basin, overlaid by the outline of our eismic data (white), the location of available wells (color coded) and the outline of the profile displayed in C. (B) The seismic-stratigraphic framework for the Southern Levant basin used in this study. (C) A depth migrated seismic cross-section through the available wells. Interpretation highlgts the seismic-stratigraphic framework and the geometry of the piano-key layer bound faults.

Figure 3: Lithological interpretation along the X-1 well. Integrating (from left to right) the seismic signature, GR log, sample cuttings, derived simplified lithology, and neutron-density log. The simplified lithology column represents the lithological variabilitty of the faulted Oligocene – Miocene section. Depth axis in this and subsequence figures were removed according to the confidentiality agreements.

Figure 4: Structural maps of the horizons used in the study, indicating the present-day geometry of the Oligocene-Miocene. Note the different depth ranges of the colour scales used for enhancing the structural elements in each map.

Figure 5: Thickness maps of the seismic-stratigraphic units used in this study. Note the different thickness ranges of colour scales used for covering the entire thickness range of each unit. The maps indicate the study area had experience two main kinematic events. The first during the Eocene, where thinning is seen across the Leviathan High. This followed by a hiatus in tectonic events druting Units 3-5 seen by an isopachous maps. The second kinematic event peaked in Unit 7, where thinning acoss the high, alongside across-fault thickening show faulting was

associated with folding. Faulting had stopped in Unit 9, but folding seem to continue unitl the deposition of the Messianian evaporites. Contours are shown for every 100 m.

Figure 6: (A) Polygonal fabric mapped across the Top Langhian structural map. (B) A cross-section through this fabric. Black arrows indicate the local depressions which form this fabric along the Top Langhian horizon; (C) A zoomed part of the map in A showing the polygonal fabric becomes concenric around the adjacent Tamar anticline; (D) A zoomed part of the map in A showing most pronaounced polygonal plan-form (white arrows); (E) A zoomed part of the map in C showing the NW-striking faults displace the polygonal fabric.

Figure 7: Cross-section through two location within the study area indicating growth-strata across the faults during the Late Burdigalian. Sections are located within (A), and away from the structural high (B), to indicate thickness changes occurred within Unit 7 regrdless of the relative location to the structural high. Syn-depositional onlaps and wedge-shape thickening are highlighted (B). Throw-depth plot for L7 fault is superimposed.

Figure 8: Flatted on Top Langhian cross-section across the Leviathan structure (A), and two zommed segments (B, C). These sections demonstrate onlapping surface within Unit 7 (dashed line) that is dated at 15 Ma (dotted line). (D) Thickness map of Unit 7b, i.e., Top Langhian (13.82 Ma) to onlapping surface (15 Ma). Folding related thickness changes are prominent, with very little faulting. (E) Thickness map of Unit 7a, i.e., Onlapping surface (15 Ma) to Intra-Burdigalian (17.54 ma). Thickness changes show very intense faulting with little folding related thinning across the structure. White dotted lines show two WSW-ENE-striking faults with high intensity of faulting around them.

Figure 9: A WSW-ENE-striking strike-slip fault. (A) An uninterpreted (left) and an interpreted (right) cross-section across the fault. A deep, singular, stem is affecting the entire sedimentary sequence in the basin with a negative flower structure developed in the younger units. (B) A thickness map of the Upper Langhian, showing thickening within the negative flower structure. (C) Left - Spectral decomposition along the Top Aquitanian horizon. Right – Simplified map of the faults along the Top Aquitanian. The maps indicates the WSW-ENE fault consists of three separate segments (marked as red faults), connected by the NW-striking faults in an en-echelon like arrangement (red arrows). Two more WSW-ENE-striking faults, located at the southern side of the Leviathan structure, are also highlighted in red arrows. The NW-striking faults are shorter, and with higher faulting intensity adjacent to the WSW-ENE faults. A dashed

line represents the northern boundary of areas of bad imaging along the Top Aquitanian horizon.

Figure 10: Geometrical properties of the faults. (A) Geographic location of the 136 mapped faults in the study area. Colours represent dip direction to the SW (red) and to the NE (blue) (B) Max throw vs fault length relative to the global database (Lathrope et al., in review). The faults are located within the global database and are not anomalous in that regard.

Figure 11: Srike-parallel throw profiles of 120 faults along the top-most horizon (Top Langhian; top) and the base horizon (Base Oligocene; bottom) with the profiles arranged into groups based on the profiles symetry (see tect for details). The resulting maps that are colour coded, mathcing with the profiles, based on the throw profiles type (centre left and right, respectively). The relative abundance of different types is shown in a pie diagram next to the respective maps. We note that unlike polygonal faults, the faults in our study area show more symmetrical profiles with depth, indicating less strain connectivity between the faults in the system.

Figure 12: Dip-parallel throw profiles of the same 120 mapeed faults. (A) left – all profiles, red line indicat the average profile. Top Right – TZ1 profiles show a substantial maximum throw along the Intra Burdigalian horizon and displacement of the entire Oligocene-Miocene sedimentary sequence. Bottom Right – TZ2 profiles show similar maximum throw along the Intra-Burdigalian horizon, but do not reach the Intra-Chattian horizon. Horizons and units depths are located based on the averaged throw profile. (B) An uninterpreted (left) and an interpreted (right) seismic profile showing TZ1 (blue) and TZ2 (red) faults. the different TZ’s. (C) Geographic location of the TZ in the study area are colour coded, mathcing with B, based on the throw profiles type. The relative abundance of different types is shown in a pie diagram next to the respctive map.

Figure 13: (A) An histogram of the Expansion Index measured for the 120 mapped faults along the eight stratigraphic units (colour coded). Syn-kinematic values are seen for the Late Burdiglian and late Langhian. Pre-kinematic values for the lower units. (B) Histograpm of the Expansion Index for the TZ1 (left) and for TZ1 (right). Values are in agreement with the thickness maps and T-Z plots, indicating that all the faults in our study area had nucleated during the Late Burdigalian as syn-depositional faults.

Figure 14: Our mechanical model for the development of the Tertiary layer-bound faults in the Levant Basin. (A) The state of stress in the early Oligocene, where NW-SE contraction

decreased, allowing isopachous deposition of Unit 3. (B&C) The states of stress developed with rapid deposition of the sand-dominated units in the Oligocene-Early Miocene, eventually creating an overpressured Eocene unit and leading to the development of a decollement layer. (D) Syn-sedimentary faults eventually nucleate during the Late Burdigalian, at the same time as slip is accommodated along the WSW-ENE-striking strike-slip fault. (E) A sketch illustrating the different elements in the Levant Basin leading to the development of the NW-striking normal faults. We propose a differential movement along the WSW-ENE-striking strike-slip faults had caused NE-trending extension, eventually leading to the development of the layer-bound faults in the Levant Basin. Faults location in the Northern Levant Basin (dashed blue line) were modified from Ghalayini and Eid (2020) (layer-bound normal faults), and from Ghalayini et al. (2014) (strike slip faults).

Figures

Figure 1

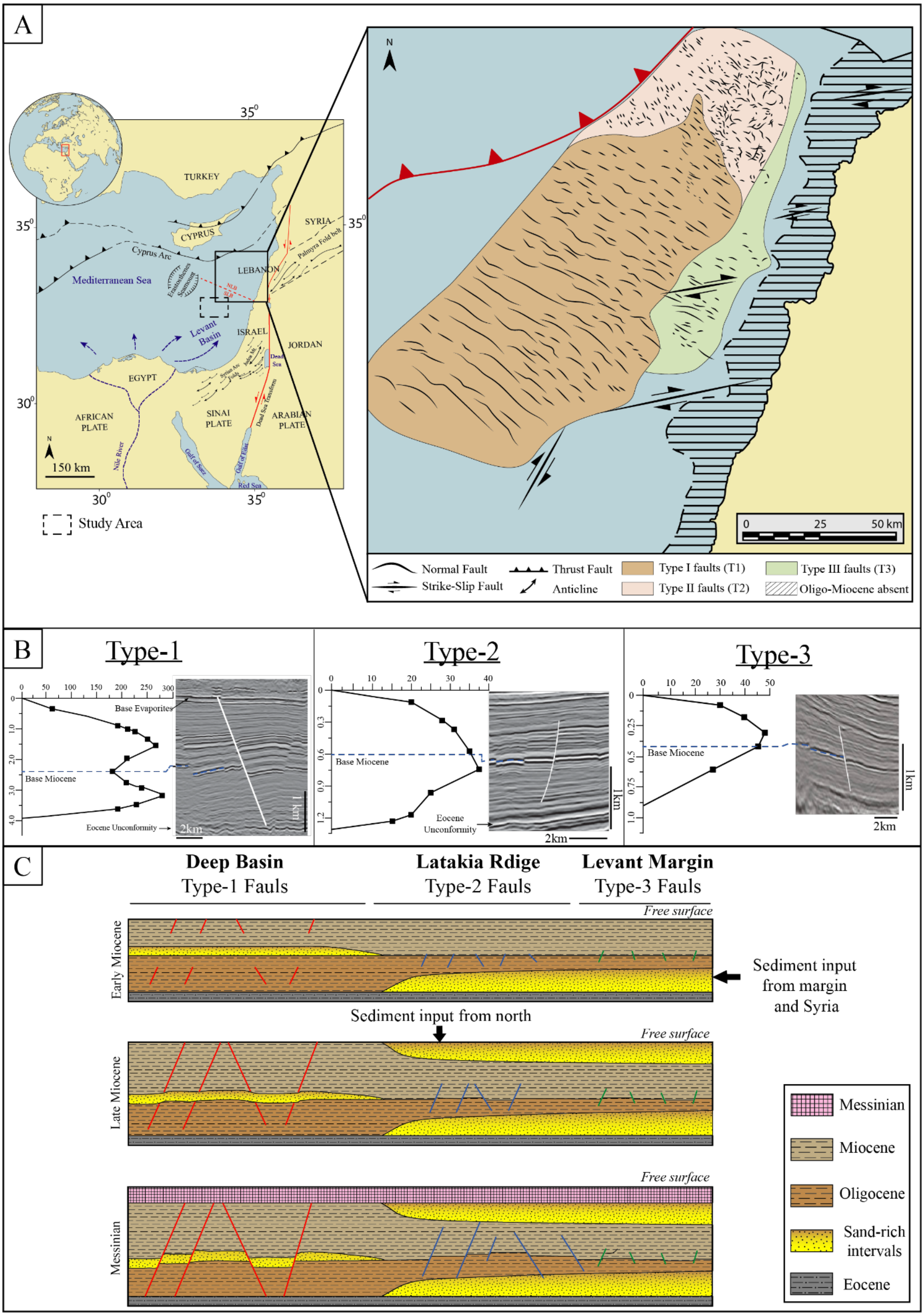

Figure 2

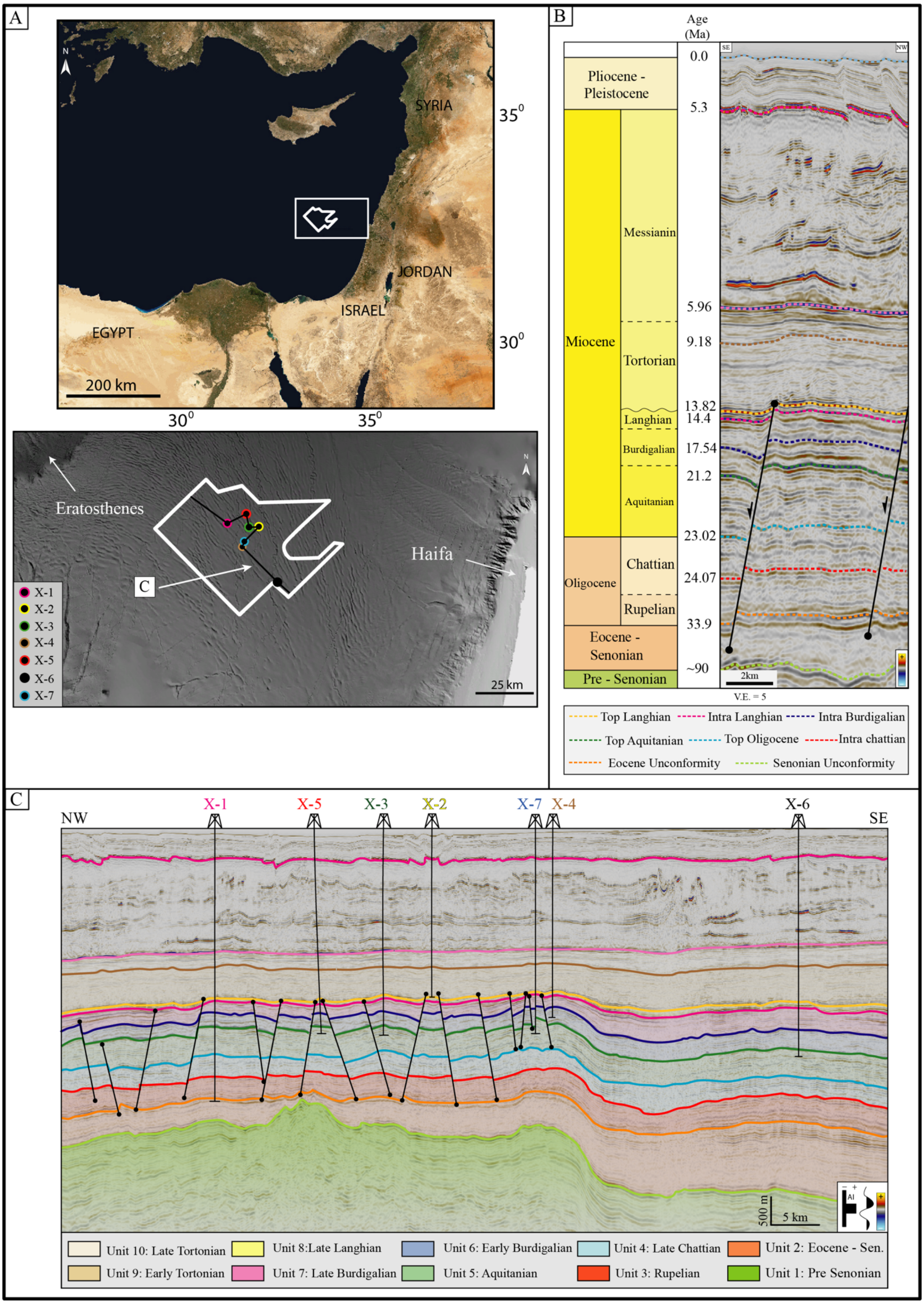

A
SYRIA
JORDAN
ISRAEL
EGYPT
35°
30°
30°
35°
200 km
Eratosthenes
Haifa
C
X-1
X-2
X-3
X-4
X-5
X-6
X-7
25 km
B
Age (Ma)
Pliocene - Pleistocene
Miocene
Messianin
Tortorian
Langhian
Burdigalian
Aquitanian
Oligocene
Chattian
Rupelian
Eocene - Senonian
Pre - Senonian
0.0
5.3
5.96
9.18
13.82
14.4
17.54
21.2
23.02
24.07
33.9
~90
SE
NW
2km
V.E. = 5
Top Langhian
Intra Langhian
Intra Burdigalian
Top Aquitanian
Top Oligocene
Intra chattian
Eocene Unconformity
Senonian Unconformity
C
NW
SE
X-1
X-5
X-3
X-2
X-7
X-4
X-6
500 m
5 km
AI
Unit 10: Late Tortonian
Unit 8:Late Langhian
Unit 6: Early Burdigalian
Unit 4: Late Chattian
Unit 2: Eocene - Sen.
Unit 9: Early Tortonian
Unit 7: Late Burdigalian
Unit 5: Aquitanian
Unit 3: Rupelian
Unit 1: Pre Senonian

1196 Figure 3

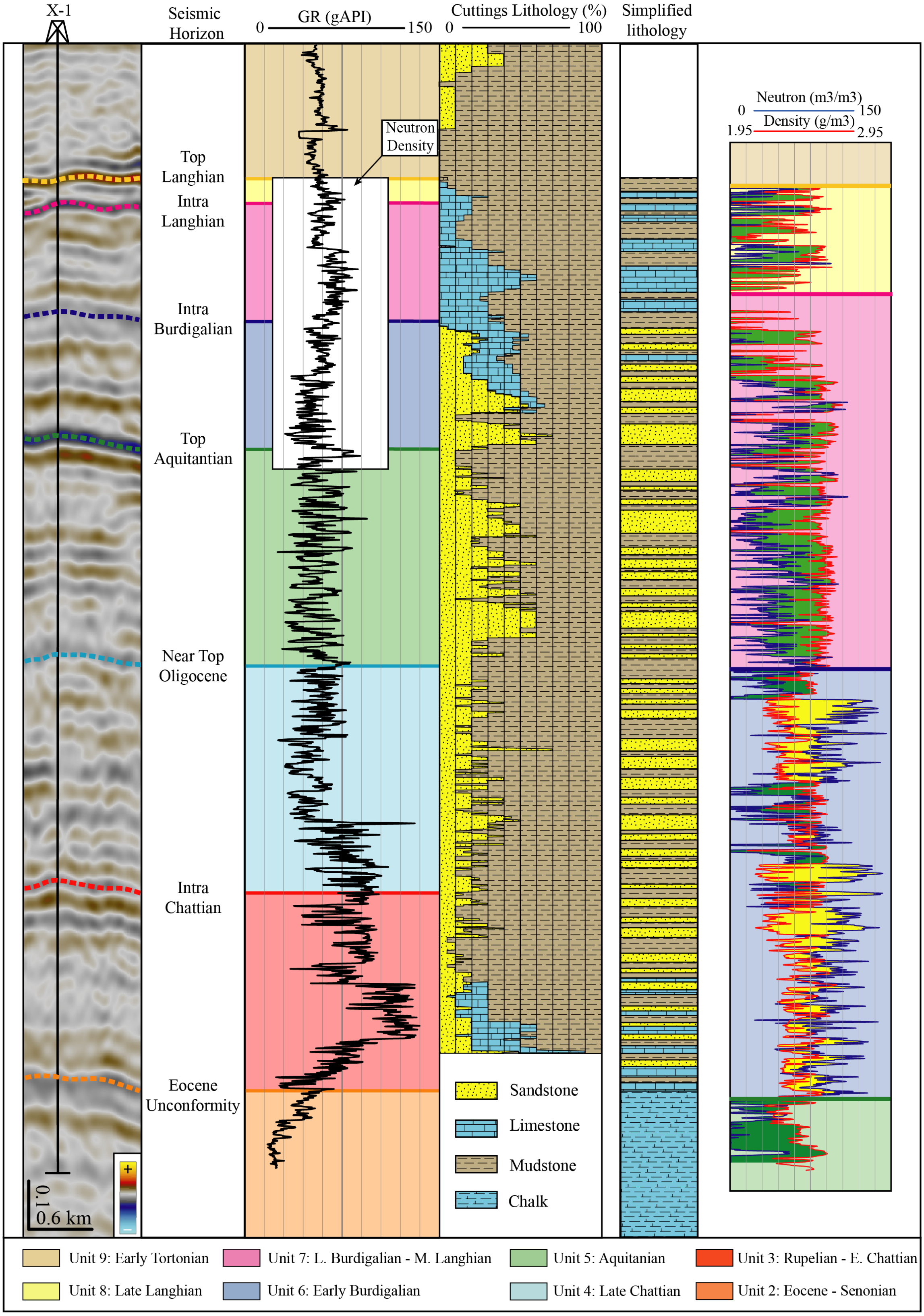

1197

Figure 4

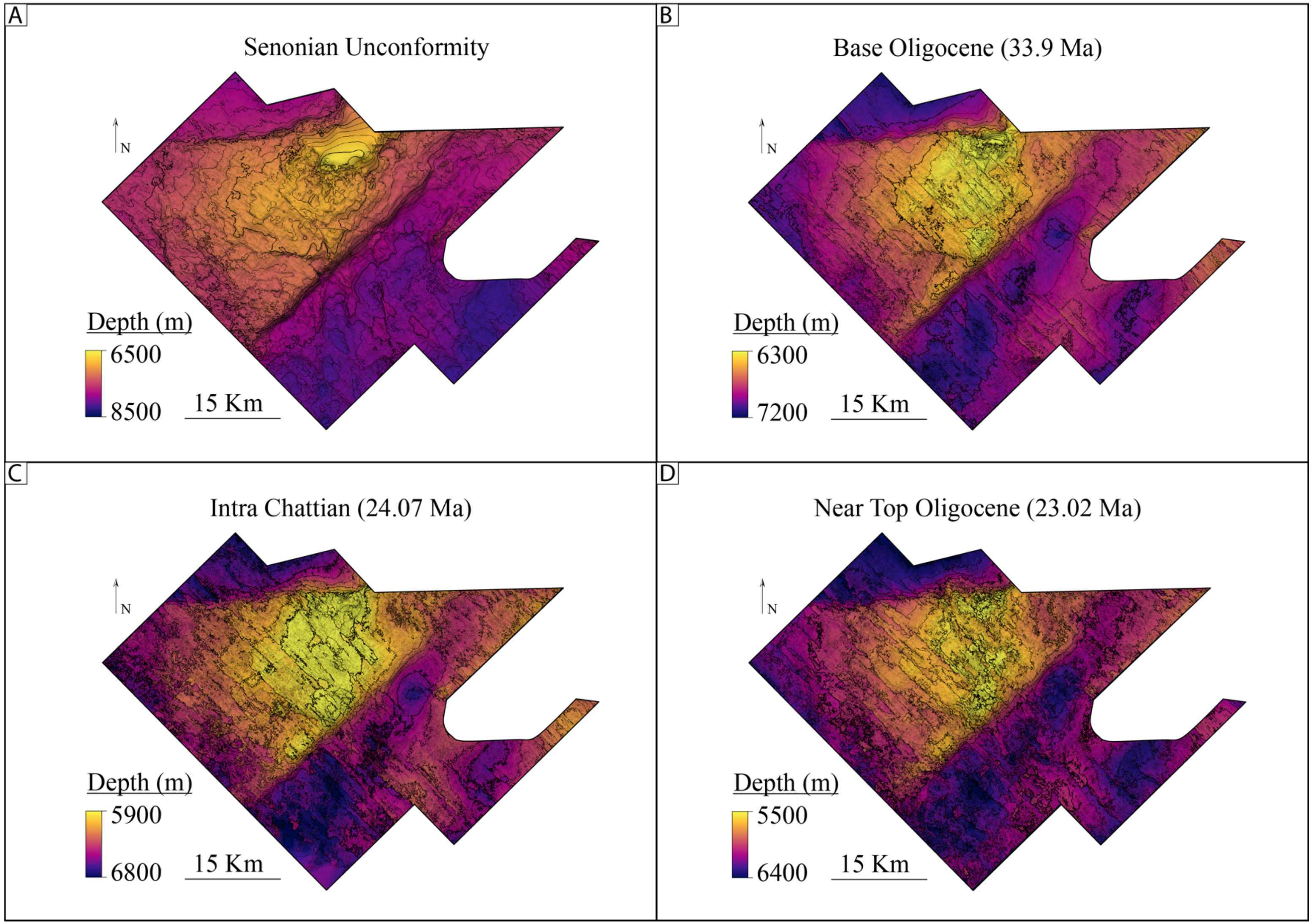
A
Senonian Unconformity
N
Depth (m)
6500
8500
15 Km
B
Base Oligocene (33.9 Ma)
N
Depth (m)
6300
7200
15 Km
C
Intra Chattian (24.07 Ma)
N
Depth (m)
5900
6800
15 Km
D
Near Top Oligocene (23.02 Ma)
N
Depth (m)
5500
6400
15 Km

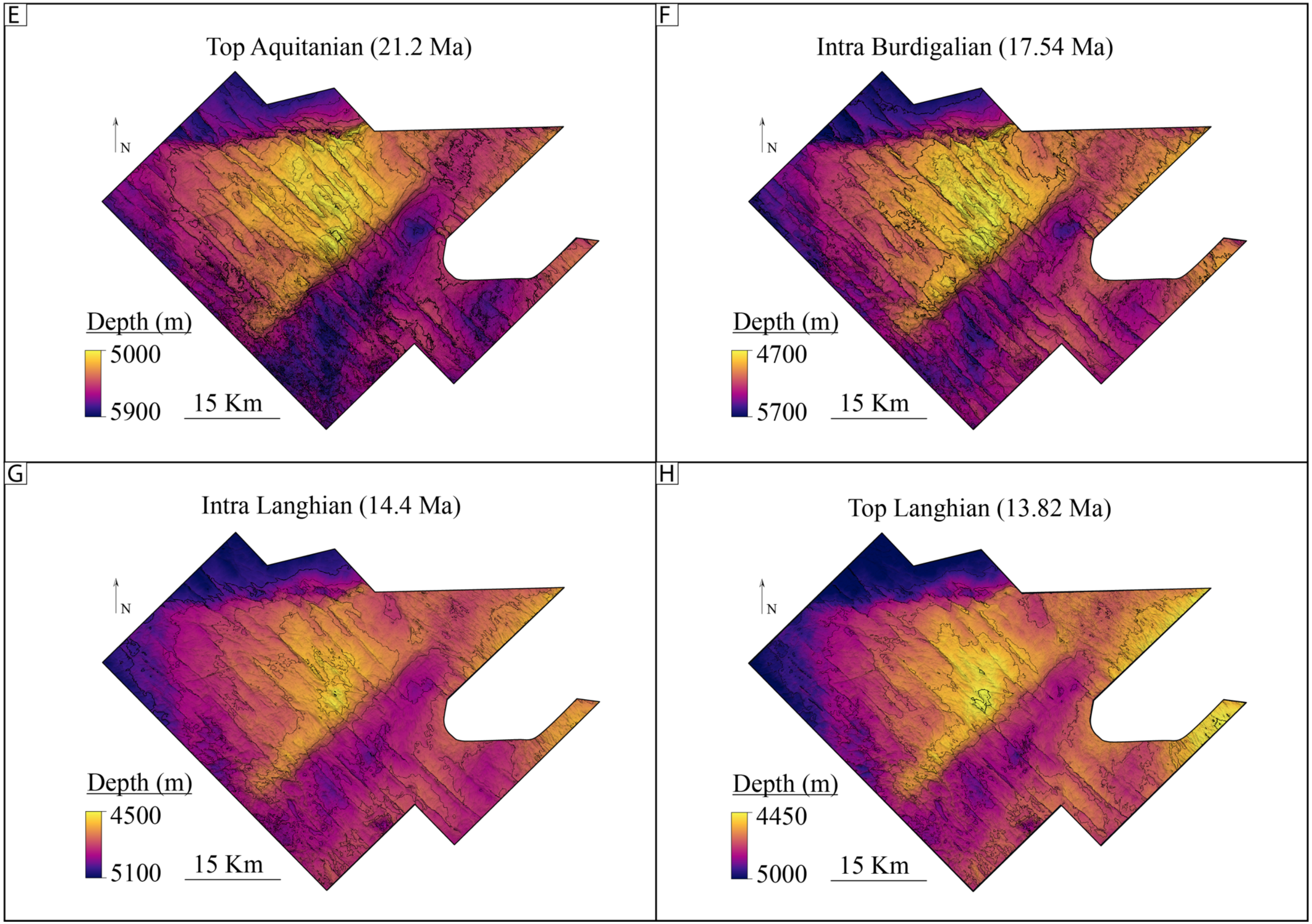
E
Top Aquitanian (21.2 Ma)
N
Depth (m)
5000
5900
15 Km
F
Intra Burdigalian (17.54 Ma)
N
Depth (m)
4700
5700
15 Km
G
Intra Langhian (14.4 Ma)
N
Depth (m)
4500
5100
15 Km
H
Top Langhian (13.82 Ma)
N
Depth (m)
4450
5000
15 Km

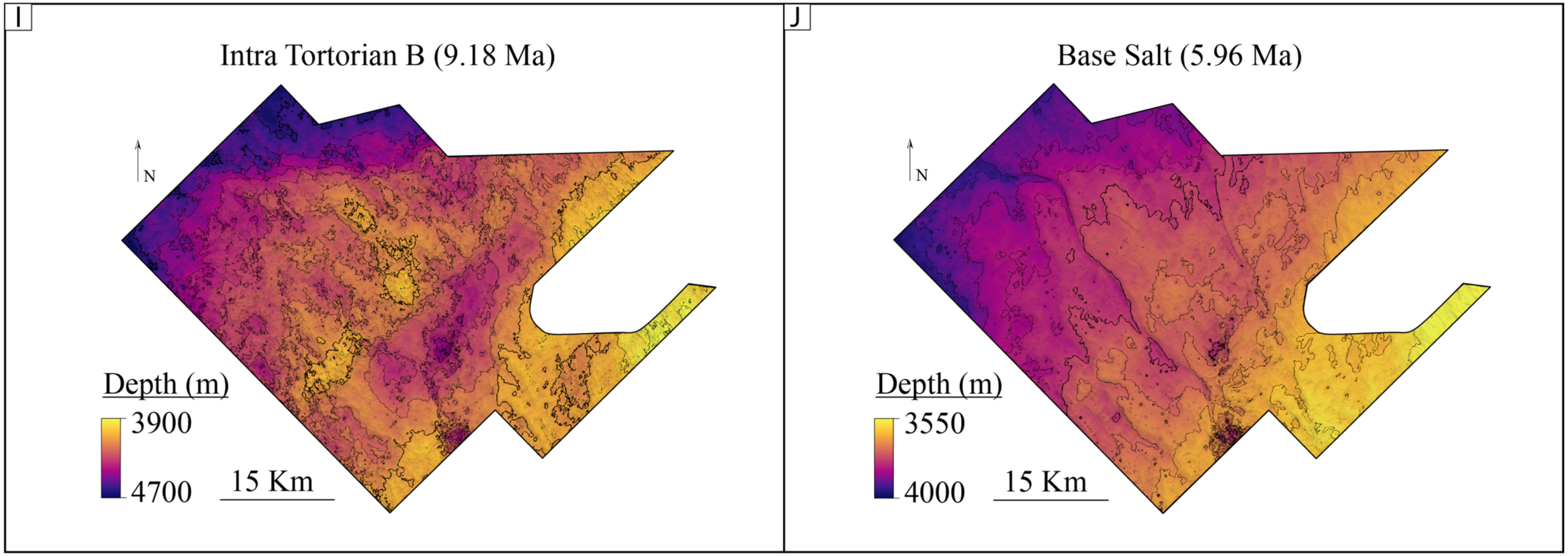
I
Intra Tortorian B (9.18 Ma)
N
Depth (m)
3900
4700
15 Km
J
Base Salt (5.96 Ma)
N
Depth (m)
3550
4000
15 Km

Figure 5

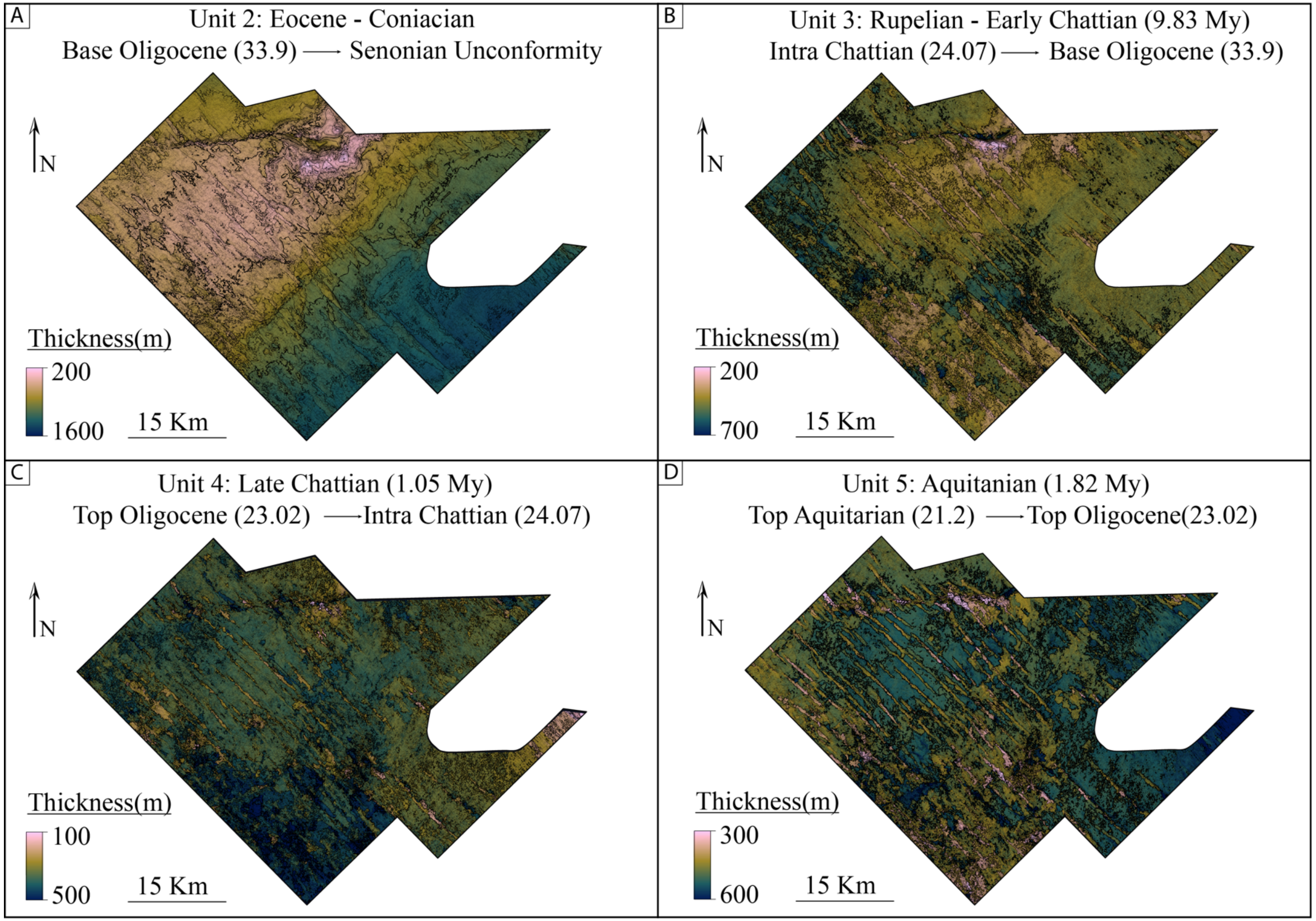
A
Unit 2: Eocene - Coniacian
Base Oligocene (33.9) ⟶ Senonian Unconformity
N
Thickness(m)
200
1600
15 Km
B
Unit 3: Rupelian - Early Chattian (9.83 My)
Intra Chattian (24.07) ⟶ Base Oligocene (33.9)
N
Thickness(m)
200
700
15 Km
C
Unit 4: Late Chattian (1.05 My)
Top Oligocene (23.02) ⟶ Intra Chattian (24.07)
N
Thickness(m)
100
500
15 Km
D
Unit 5: Aquitanian (1.82 My)
Top Aquitanian (21.2) ⟶ Top Oligocene(23.02)
N
Thickness(m)
300
600
15 Km

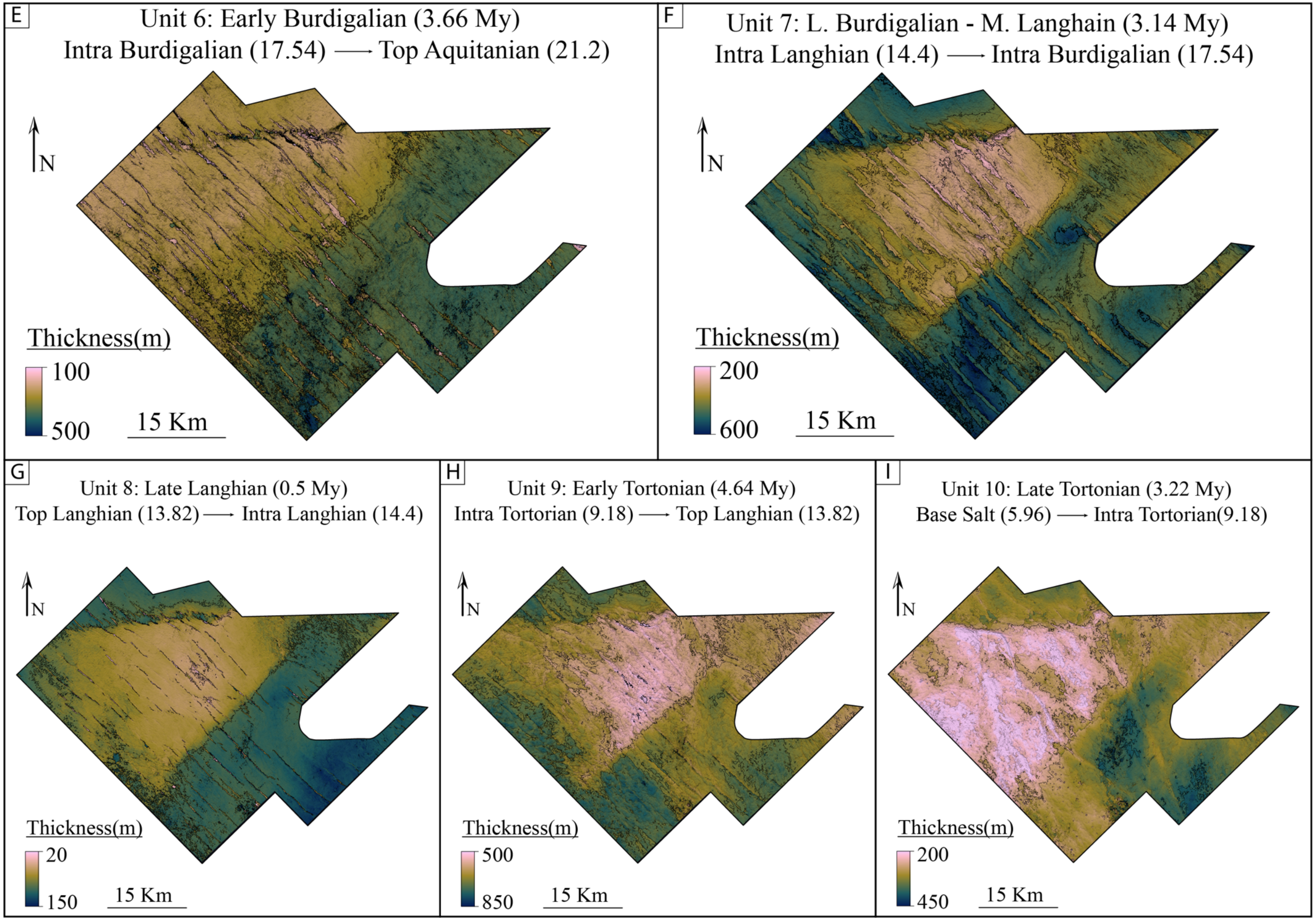
E
Unit 6: Early Burdigalian (3.66 My)
Intra Burdigalian (17.54) ⟶ Top Aquitanian (21.2)
N
Thickness(m)
100
500
15 Km
F
Unit 7: L. Burdigalian - M. Langhain (3.14 My)
Intra Langhian (14.4) ⟶ Intra Burdigalian (17.54)
N
Thickness(m)
200
600
15 Km
G
Unit 8: Late Langhian (0.5 My)
Top Langhian (13.82) ⟶ Intra Langhian (14.4)
N
Thickness(m)
20
150
15 Km
H
Unit 9: Early Tortonian (4.64 My)
Intra Tortorian (9.18) ⟶ Top Langhian (13.82)
N
Thickness(m)
500
850
15 Km
I
Unit 10: Late Tortonian (3.22 My)
Base Salt (5.96) ⟶ Intra Tortorian(9.18)
N
Thickness(m)
200
450
15 Km

Figure 6

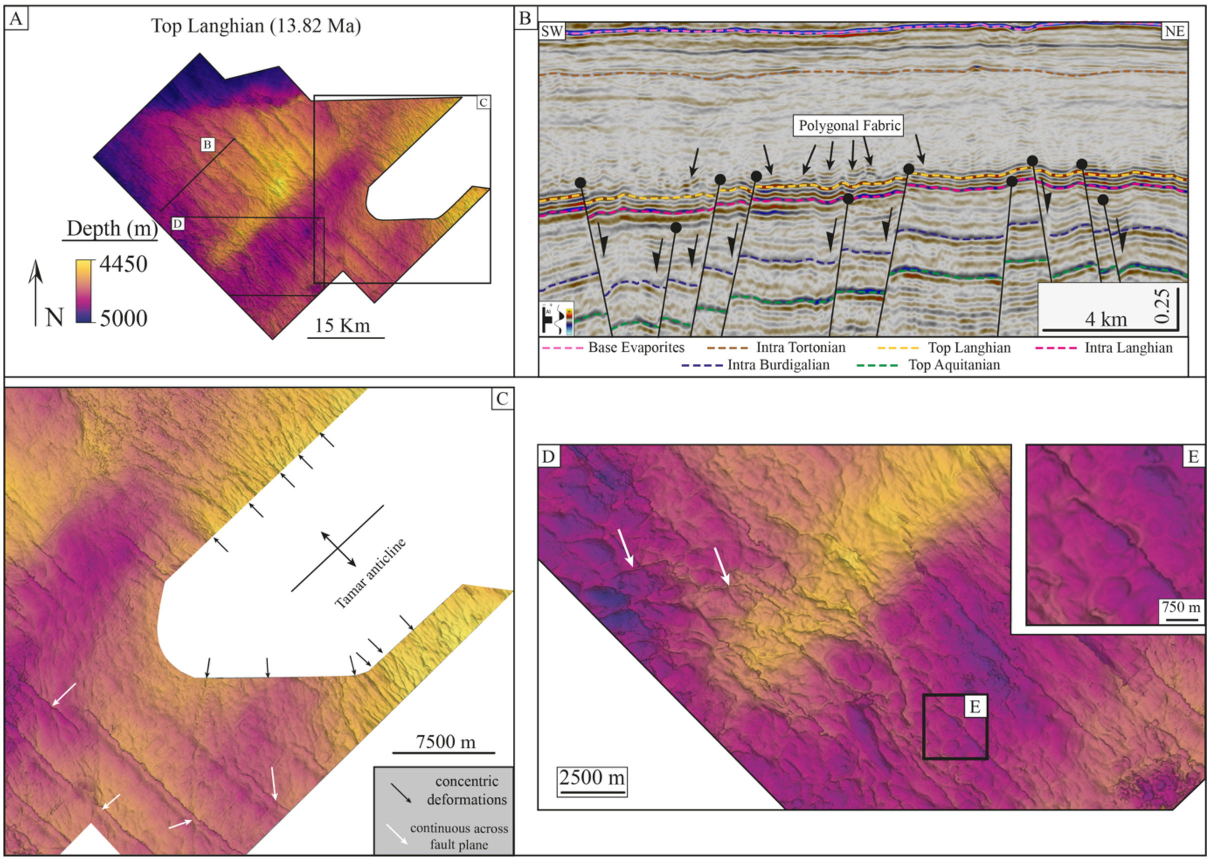

A
Top Langhian (13.82 Ma)
Depth (m)
4450
5000
N
15 Km
B
SW
NE
Polygonal Fabric
4 km
0.25
Base Evaporites
Intra Tortonian
Top Langhian
Intra Langhian
Intra Burdigalian
Top Aquitanian
C
Tamar anticline
7500 m
concentric deformations
continuous across fault plane
D
E
2500 m
750 m

Figure 7

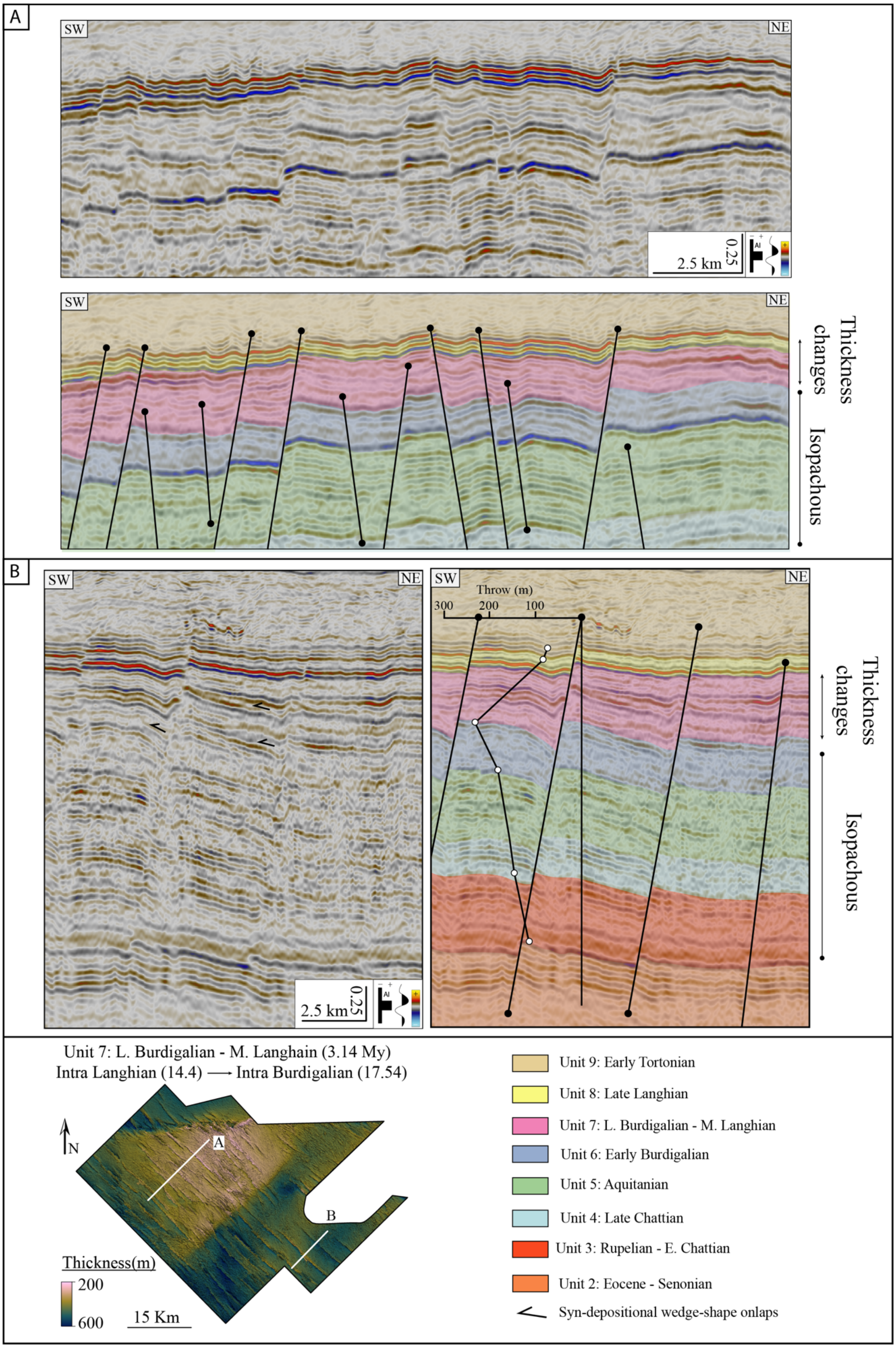
A
SW
NE
2.5 km
0.25
Thickness changes
Isopachous
B
Throw (m)
300
200
100
Unit 7: L. Burdigalian - M. Langhain (3.14 My)
Intra Langhian (14.4) ⟶ Intra Burdigalian (17.54)
N
Thickness(m)
200
600
15 Km
Unit 9: Early Tortonian
Unit 8: Late Langhian
Unit 7: L. Burdigalian - M. Langhian
Unit 6: Early Burdigalian
Unit 5: Aquitanian
Unit 4: Late Chattian
Unit 3: Rupelian - E. Chattian
Unit 2: Eocene - Senonian
Syn-depositional wedge-shape onlaps

1212 Figure 8

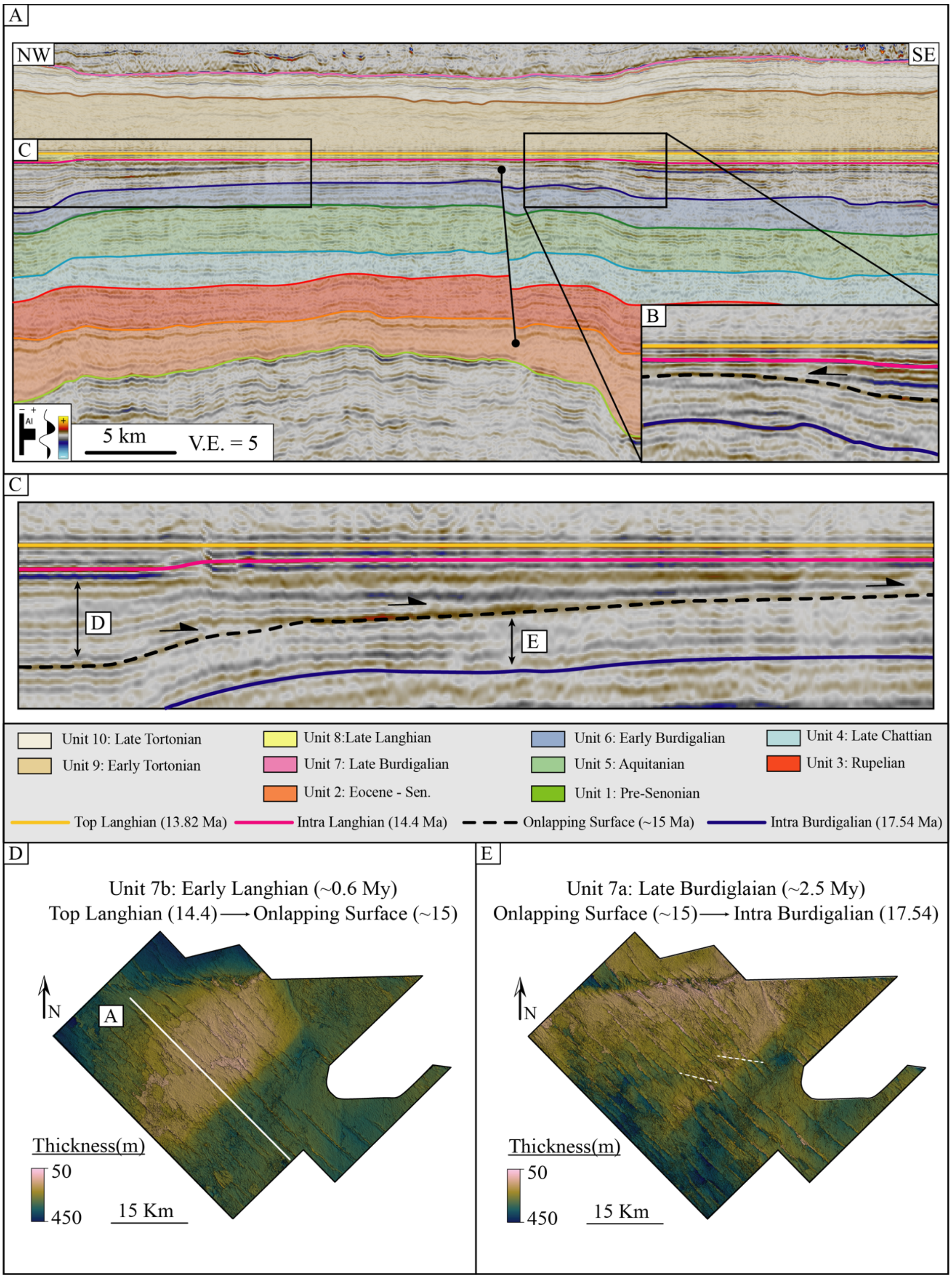

1213

Figure 9

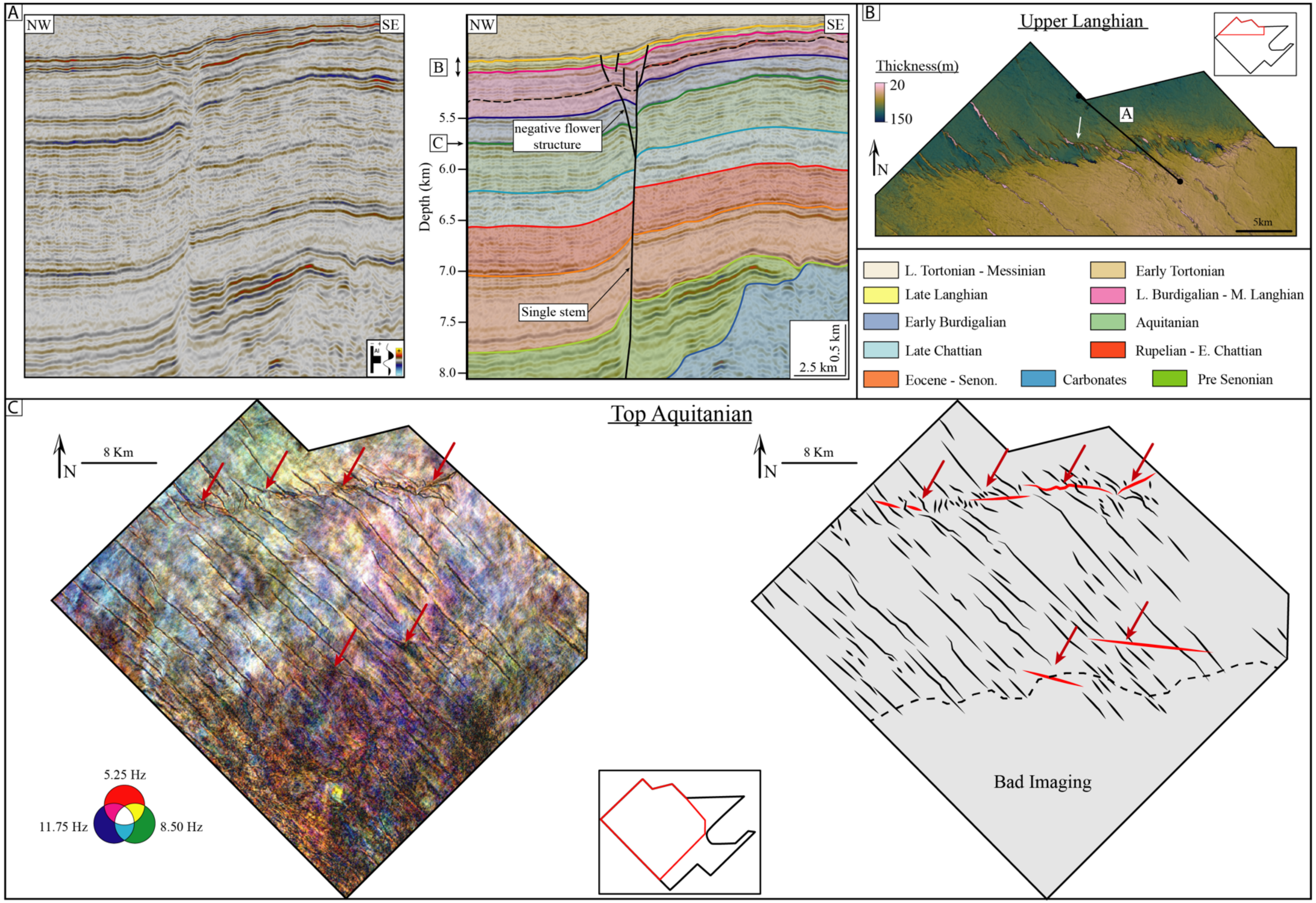
A
NW
SE
NW
SE
B
C
5.5
6.0
6.5
7.0
7.5
8.0
Depth (km)
negative flower structure
Single stem
0.5 km
2.5 km
B
Upper Langhian
Thickness(m)
20
150
A
N
5km
L. Tortonian - Messinian
Early Tortonian
Late Langhian
L. Burdigalian - M. Langhian
Early Burdigalian
Aquitanian
Late Chattian
Rupelian - E. Chattian
Eocene - Senon.
Carbonates
Pre Senonian
C
Top Aquitanian
N
8 Km
5.25 Hz
11.75 Hz
8.50 Hz
N
8 Km
Bad Imaging

Figure 10

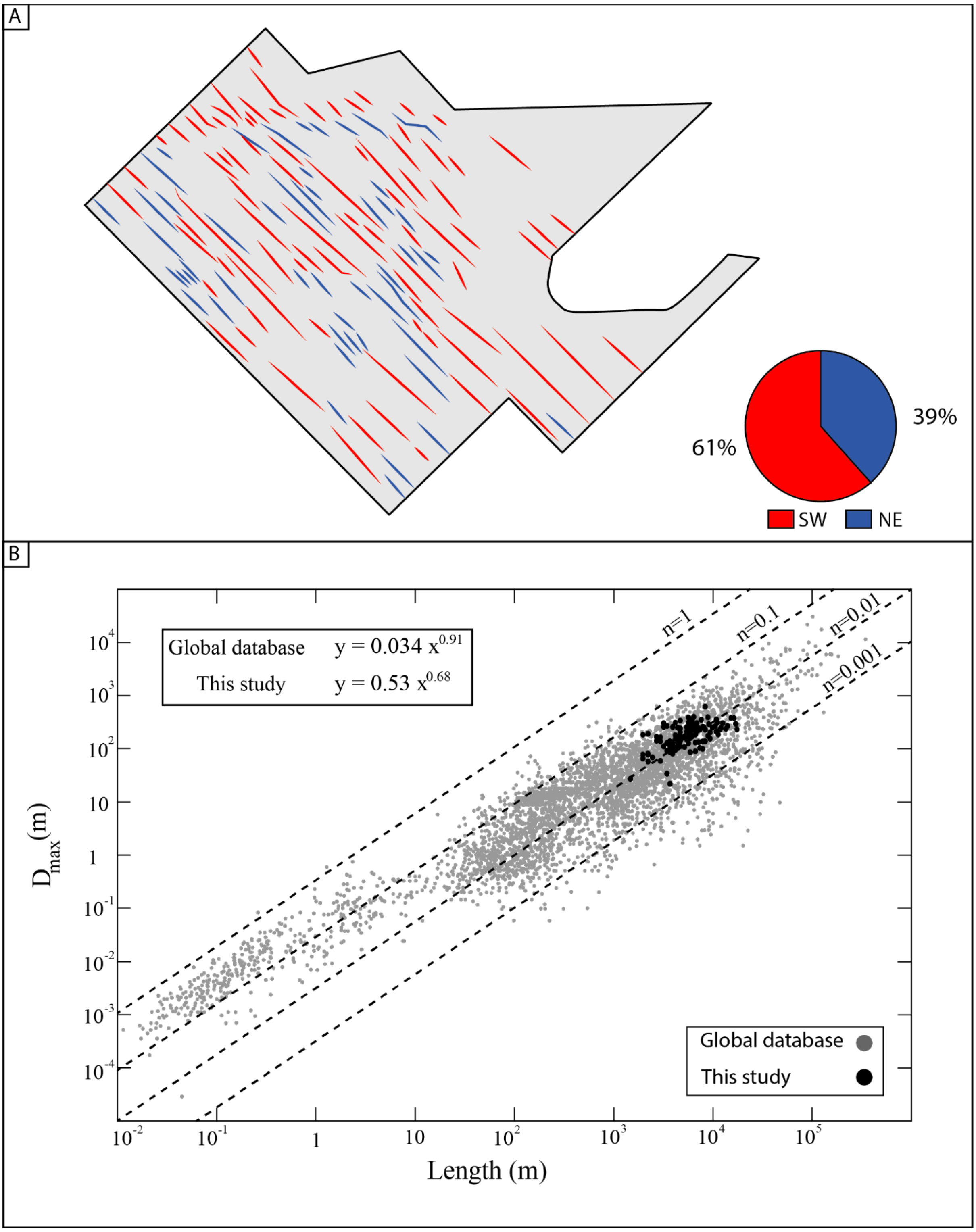
A
61%
39%
SW
NE
B
Global database y = 0.034 x^0.91
This study y = 0.53 x^0.68
n=1
n=0.1
n=0.01
n=0.001
D_max (m)
10^4
10^3
10^2
10
1
10^-1
10^-2
10^-3
10^-4
10^-2
10^-1
1
10
10^2
10^3
10^4
10^5
Length (m)
Global database
This study

Figure 11

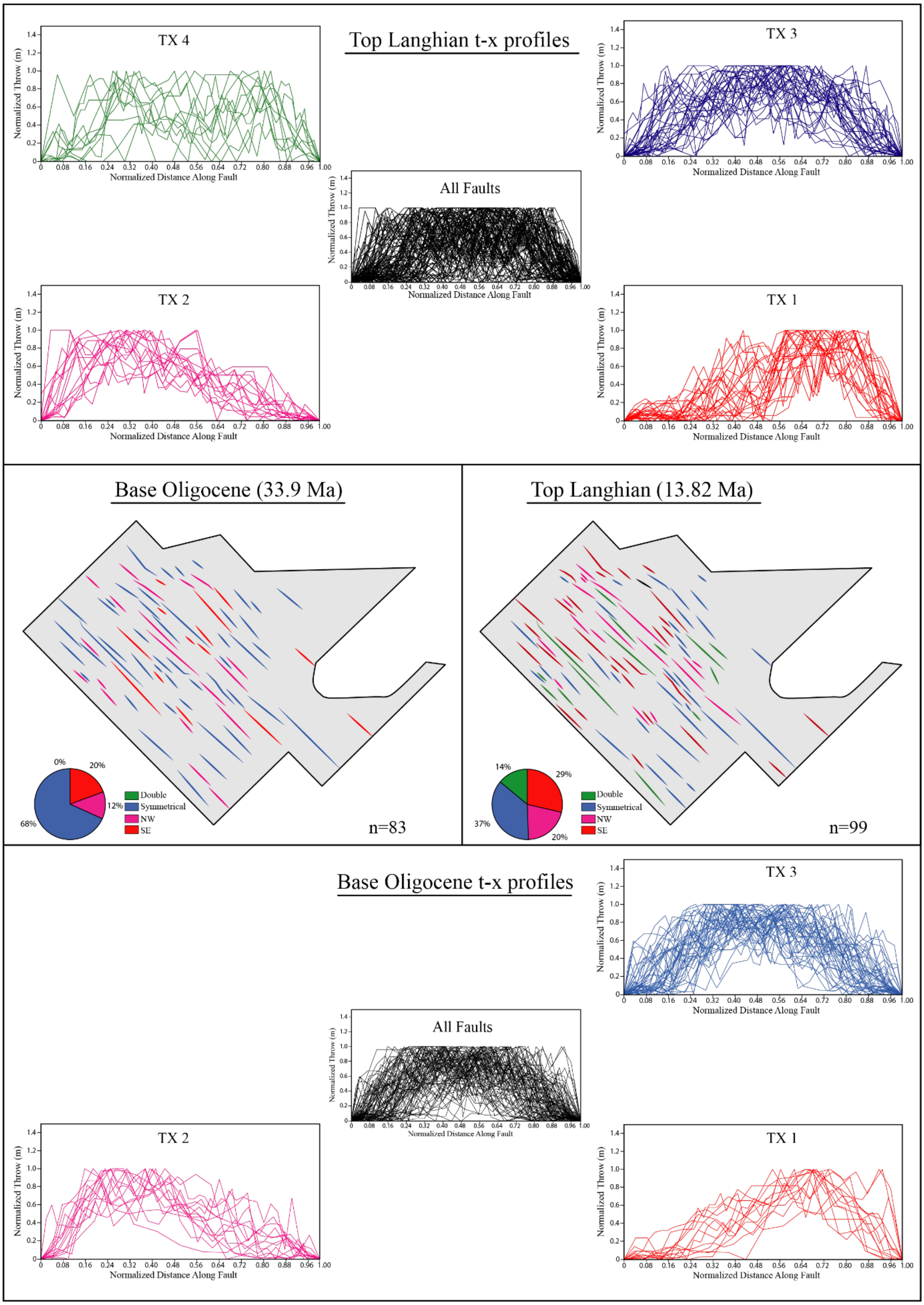

Top Langhian t-x profiles
TX 4
TX 3
All Faults
TX 2
TX 1
Normalized Throw (m)
Normalized Distance Along Fault
Base Oligocene (33.9 Ma)
Top Langhian (13.82 Ma)
0%
20%
12%
68%
14%
29%
20%
37%
Double
Symmetrical
NW
SE
n=83
n=99
Base Oligocene t-x profiles

1223 Figure 12

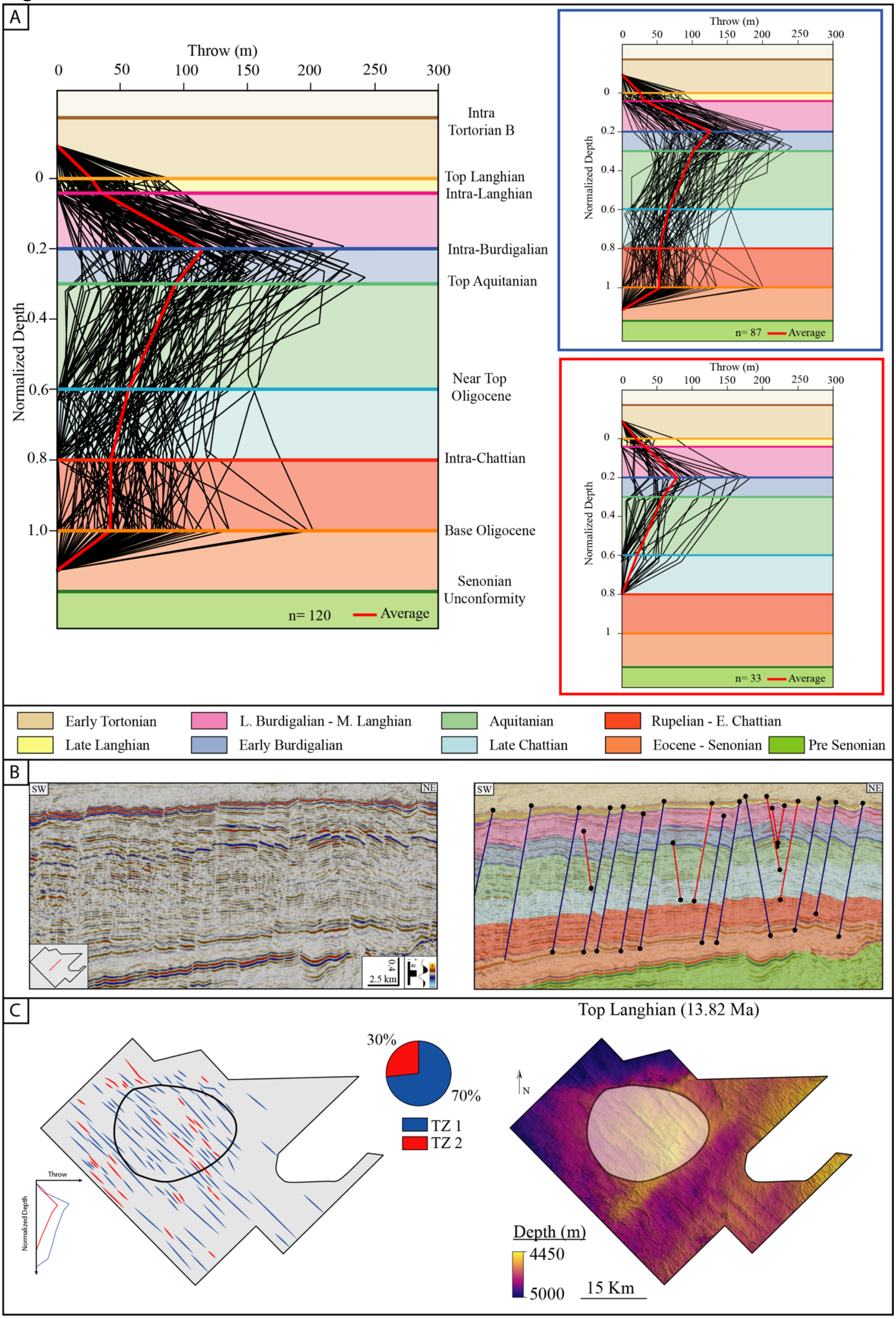

1224

Figure 13

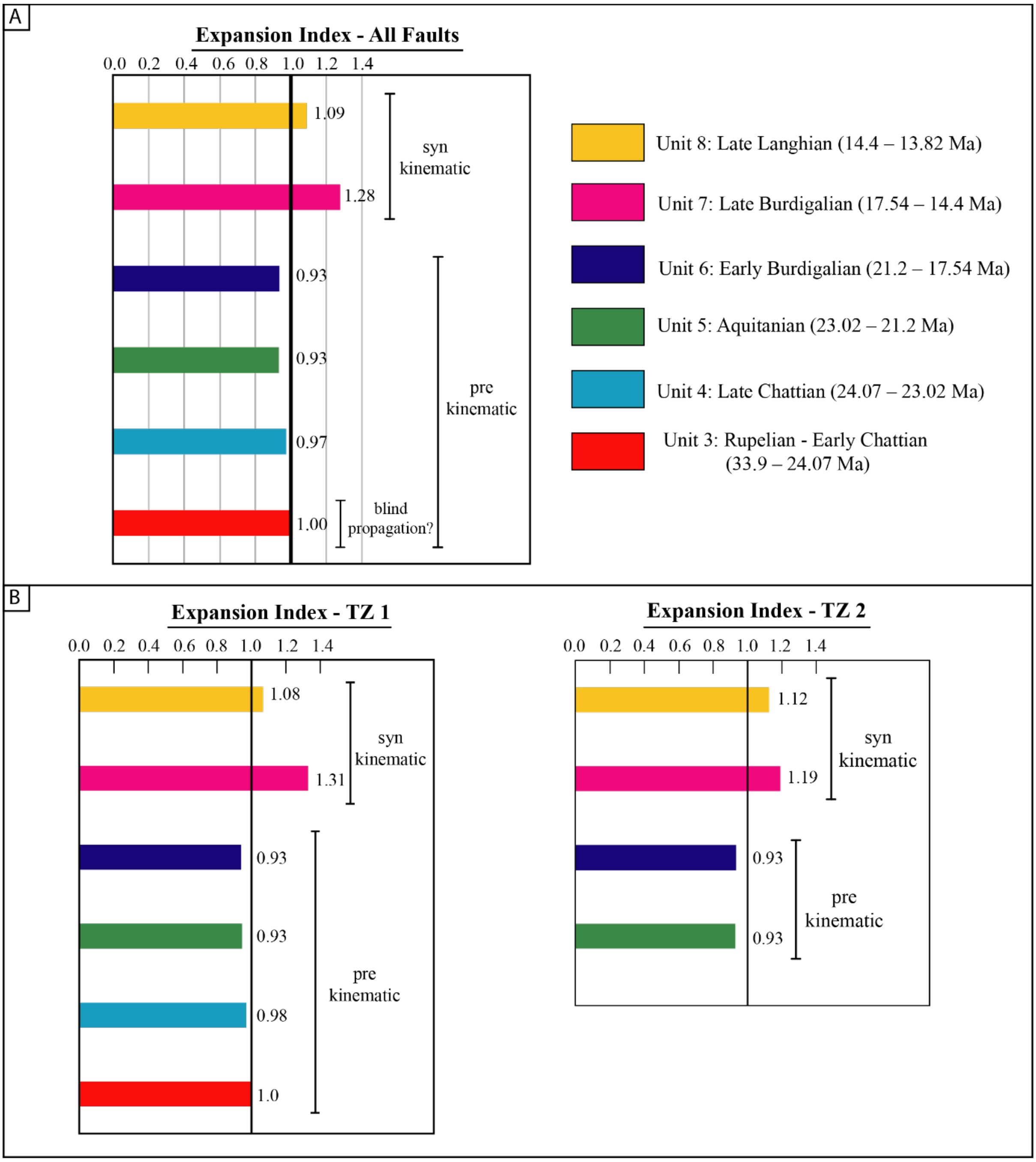

A
Expansion Index - All Faults
0.0 0.2 0.4 0.6 0.8 1.0 1.2 1.4
1.09
1.28
0.93
0.93
0.97
1.00
syn kinematic
pre kinematic
blind propagation?
Unit 8: Late Langhian (14.4 – 13.82 Ma)
Unit 7: Late Burdigalian (17.54 – 14.4 Ma)
Unit 6: Early Burdigalian (21.2 – 17.54 Ma)
Unit 5: Aquitanian (23.02 – 21.2 Ma)
Unit 4: Late Chattian (24.07 – 23.02 Ma)
Unit 3: Rupelian - Early Chattian (33.9 – 24.07 Ma)
B
Expansion Index - TZ 1
0.0 0.2 0.4 0.6 0.8 1.0 1.2 1.4
1.08
1.31
0.93
0.93
0.98
1.0
syn kinematic
pre kinematic
Expansion Index - TZ 2
0.0 0.2 0.4 0.6 0.8 1.0 1.2 1.4
1.12
1.19
0.93
0.93
syn kinematic
pre kinematic

Figure 14

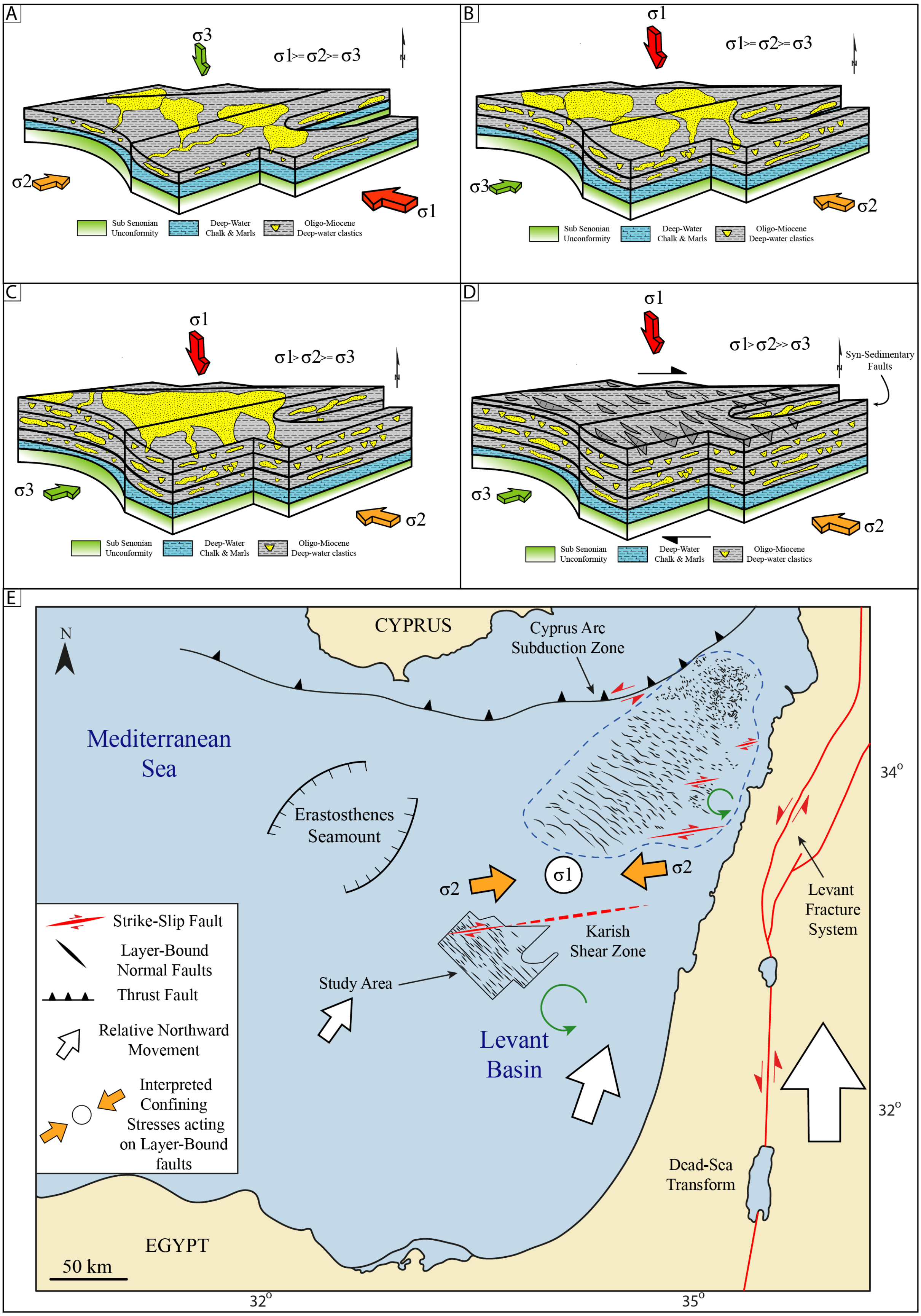
A
σ3
σ1>=σ2>=σ3
σ2
σ1
Sub Senonian Unconformity
Deep-Water Chalk & Marls
Oligo-Miocene Deep-water clastics
B
σ1
σ1>=σ2>=σ3
σ3
σ2
Sub Senonian Unconformity
Deep-Water Chalk & Marls
Oligo-Miocene Deep-water clastics
C
σ1
σ1>σ2>=σ3
σ3
σ2
Sub Senonian Unconformity
Deep-Water Chalk & Marls
Oligo-Miocene Deep-water clastics
D
σ1
σ1>σ2>>σ3
Syn-Sedimentary Faults
σ3
σ2
Sub Senonian Unconformity
Deep-Water Chalk & Marls
Oligo-Miocene Deep-water clastics
E
N
CYPRUS
Cyprus Arc Subduction Zone
Mediterranean Sea
Erastosthenes Seamount
34°
σ2
σ1
σ2
Levant Fracture System
Karish Shear Zone
Study Area
Levant Basin
32°
Dead-Sea Transform
EGYPT
50 km
32°
35°
Strike-Slip Fault
Layer-Bound Normal Faults
Thrust Fault
Relative Northward Movement
Interpreted Confining Stresses acting on Layer-Bound faults

Supplementary Information

Neutron Density

Original wireline data provided to this study, and other references (e.g., Christensen and Powers (2013)), are all sandstone calibrated, and not limestone calibrated as most published data. To make it easier to the reader to understand the wireline interpretation, we converted the calibration from sandstone to limestone using IP software.

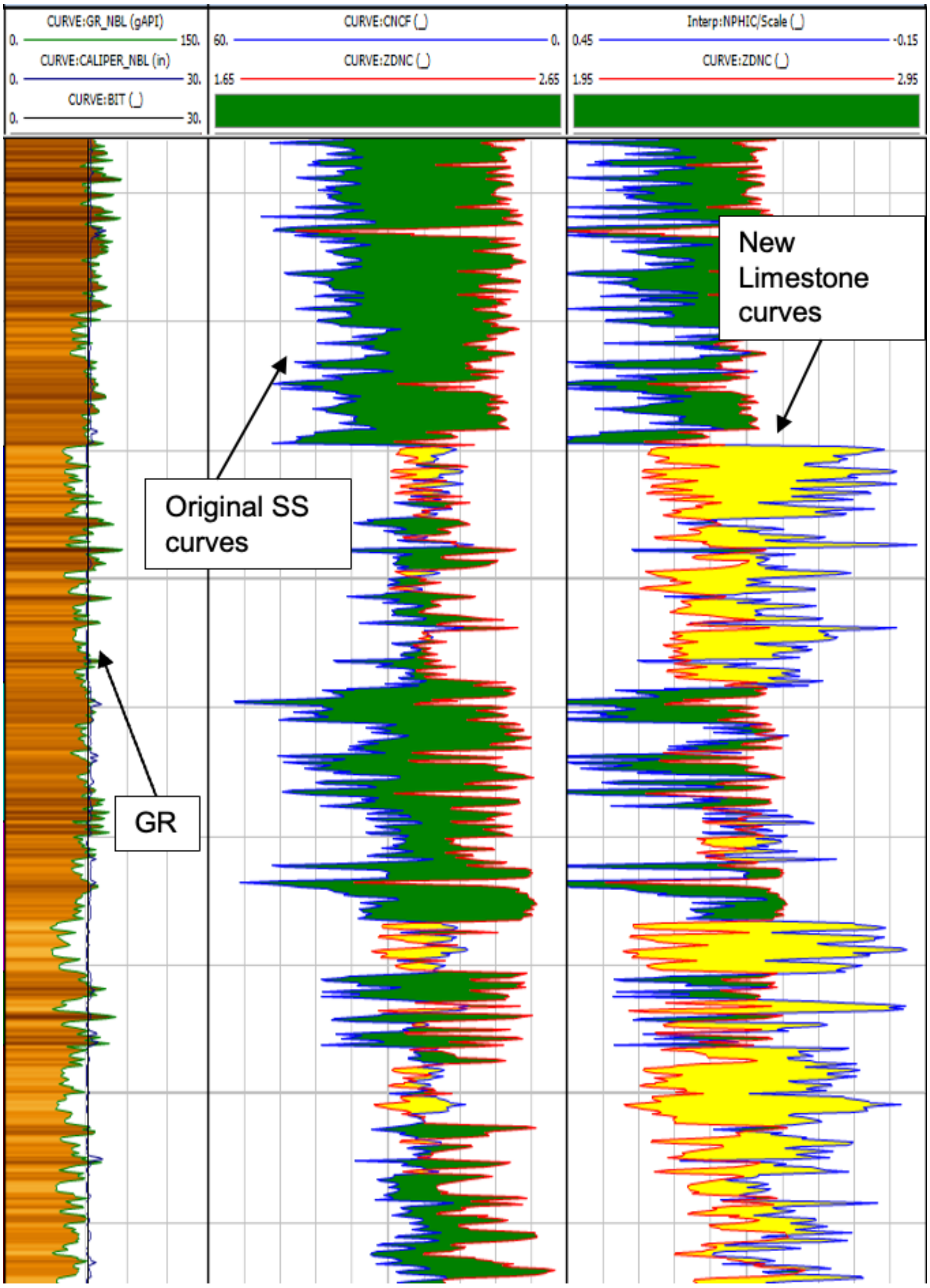

Throw – length (T-X) profiles for each horizon not listed on Figure 11

Intra Langhian horizon

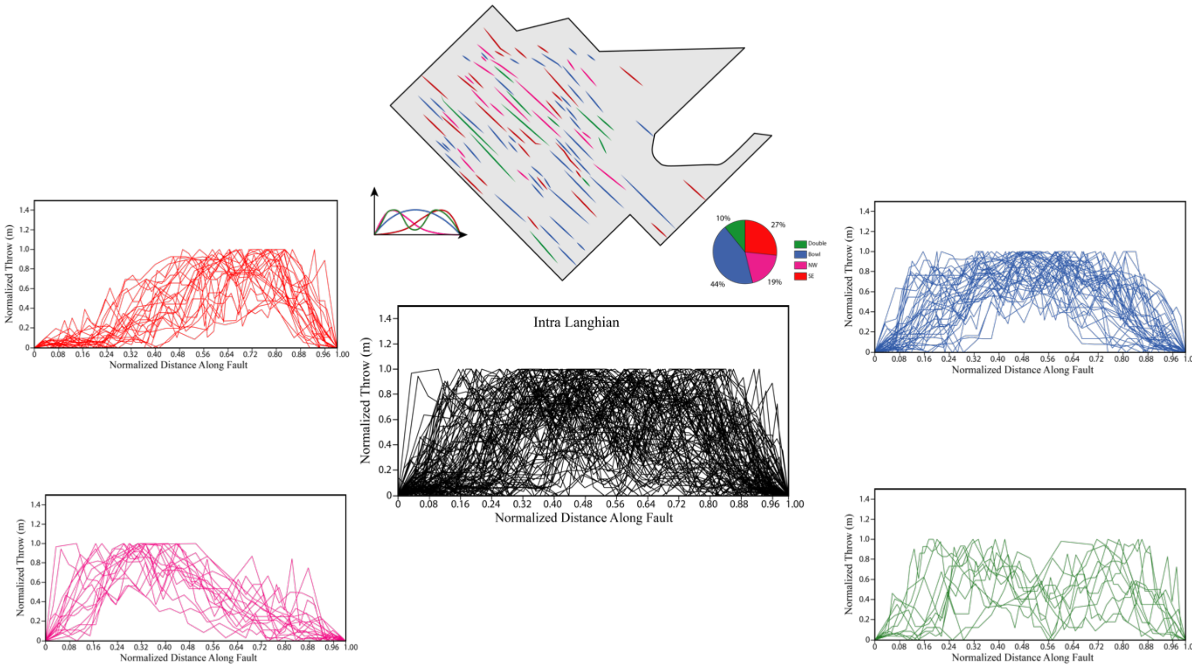

Intra Burdigalian

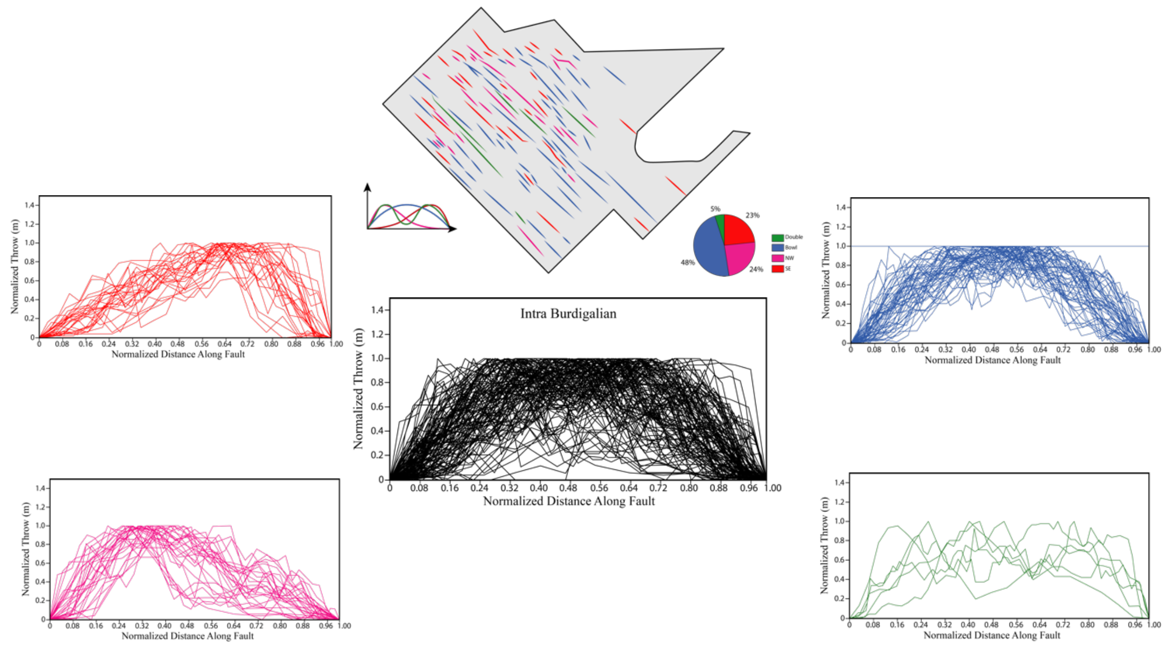

Top Aquitanian

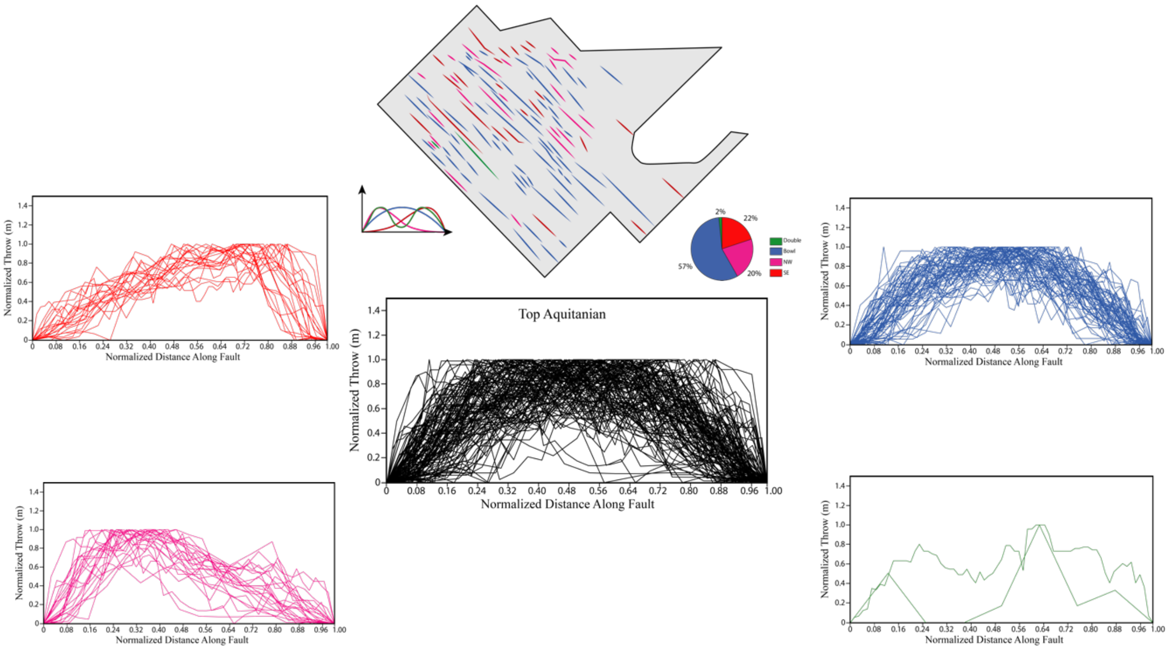

Near Top Oligocene

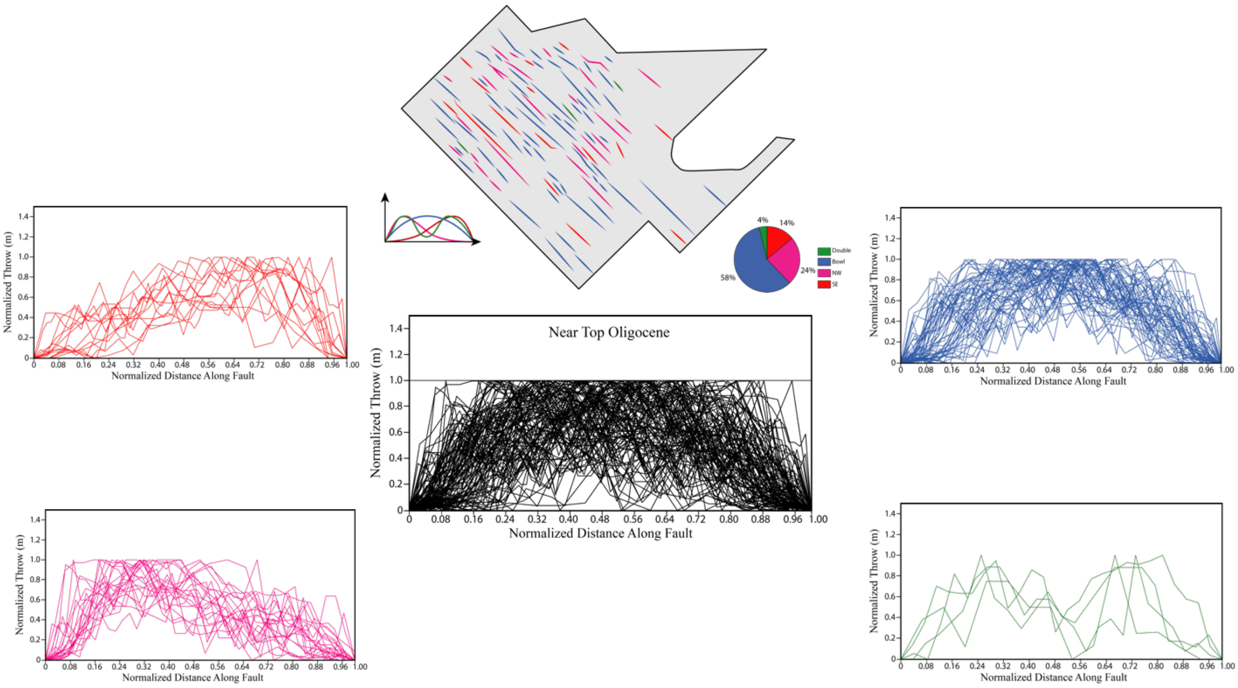

Intra Chattian

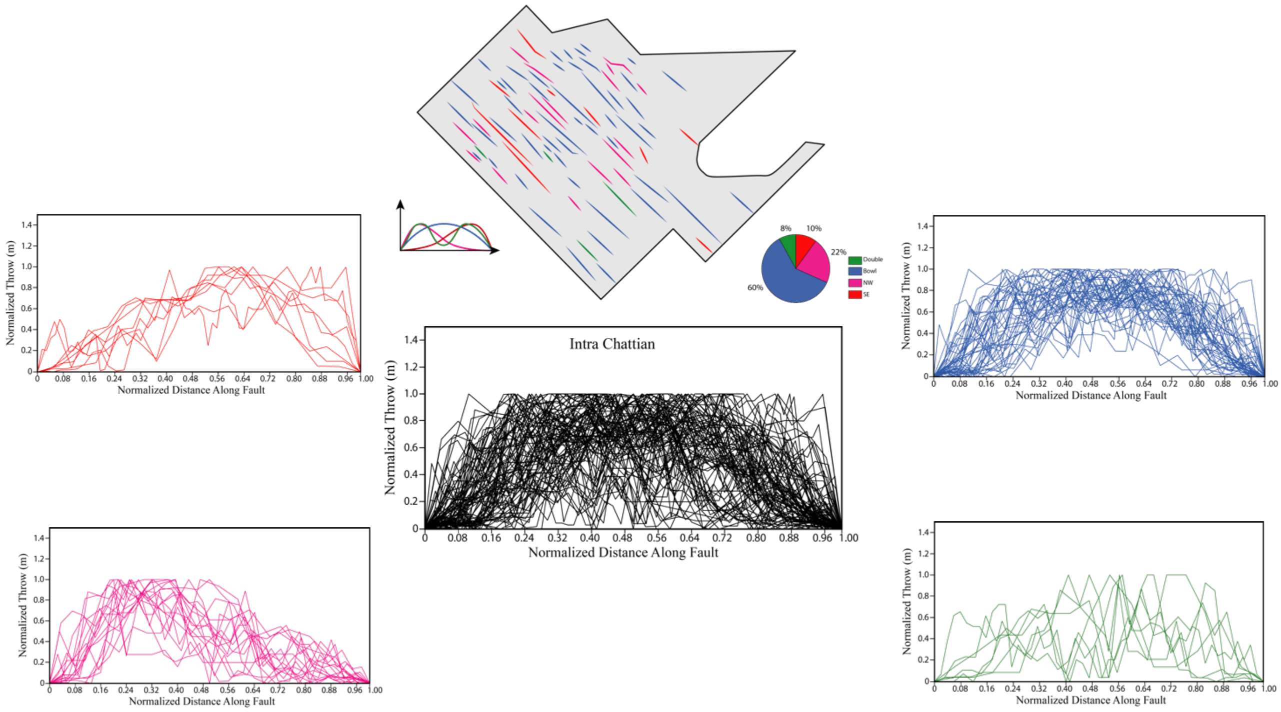

Intra Chattian
Normalized Throw (m)
Normalized Distance Along Fault
Double
Bowl
NW
SE
8%
10%
22%
60%